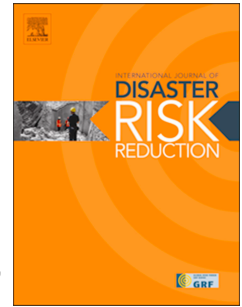


# Journal Pre-proof

A Stochastic Rain-on-Grid Framework for Handling Spatio-Temporal Rainfall Uncertainty in Impact-based Flood Nowcasting

Pierfranco Costabile, Margherita Lombardo, Carmelina Costanzo, Ioannis Tsoukalas, Vasilis Bellos



PII: S2212-4209(26)00010-5

DOI: <https://doi.org/10.1016/j.ijdr.2026.105998>

Reference: IJDRR 105998

To appear in: *International Journal of Disaster Risk Reduction*

Received Date: 12 November 2025

Revised Date: 6 January 2026

Accepted Date: 6 January 2026

Please cite this article as: P. Costabile, M. Lombardo, C. Costanzo, I. Tsoukalas, V. Bellos, A Stochastic Rain-on-Grid Framework for Handling Spatio-Temporal Rainfall Uncertainty in Impact-based Flood Nowcasting, *International Journal of Disaster Risk Reduction*, <https://doi.org/10.1016/j.ijdr.2026.105998>.

This is a PDF of an article that has undergone enhancements after acceptance, such as the addition of a cover page and metadata, and formatting for readability. This version will undergo additional copyediting, typesetting and review before it is published in its final form. As such, this version is no longer the Accepted Manuscript, but it is not yet the definitive Version of Record; we are providing this early version to give early visibility of the article. Please note that Elsevier's sharing policy for the Published Journal Article applies to this version, see: <https://www.elsevier.com/about/policies-and-standards/sharing#4-published-journal-article>. Please also note that, during the production process, errors may be discovered which could affect the content, and all legal disclaimers that apply to the journal pertain.

© 2026 Published by Elsevier Ltd.

1        A Stochastic Rain-on-Grid Framework for Handling Spatio-  
2        Temporal Rainfall Uncertainty in Impact-based Flood Nowcasting

3        Pierfranco Costabile<sup>1</sup>, Margherita Lombardo<sup>1</sup>, Carmelina Costanzo<sup>1</sup>,  
4        Ioannis Tsoukalas<sup>2</sup>, Vasilis Bellos<sup>3</sup>

5        <sup>1</sup>Department of Environmental Engineering, University of Calabria, Rende (CS), Italy

6        <sup>2</sup>Department of Civil Engineering, Democritus University of Thrace, Xanthi, Greece

7        <sup>3</sup>Department of Environmental Engineering, Democritus University of Thrace, Xanthi, Greece

8        Corresponding author: Pierfranco Costabile, pierfranco.costabile@unical.it

## 9 Abstract

10 Predicting flash flood impacts remains a major challenge due to intrinsic uncertainty in rainfall spatial-temporal structure  
11 and limited understanding of how rainfall organization propagates through hydrological and hydrodynamic processes to  
12 generate urban-scale impacts. These limitations hinder the development of reliable impact-based early warning systems  
13 for small, fast-responding catchments.

14 To address these challenges, we introduce a Stochastic Rain-on-Grid framework that explicitly accounts for rainfall  
15 uncertainty by coupling a high-resolution stochastic rainfall generator with a 2D hydrodynamic model operating at the  
16 watershed scale. The framework is applied to a representative high-impact flash flood event affecting a piedmont  
17 urbanized area characterized by complex interactions between mountain and urban flooding processes. Using 100  
18 equiprobable synthetic storms reproducing the statistical properties of the observed radar rainfall (200 m, 2 min), we  
19 assess how rainfall spatio-temporal variability alone influences catchment response and street-level flood impacts.

20 Results show substantial variability in simulated hydrographs despite statistically similar rainfall inputs, while this  
21 variability systematically attenuates at the street scale, leading to more stable hazard classifications. This indicates that  
22 impact-based hydrodynamic indicators are more robust targets for early warning systems than traditional hydrograph-  
23 based metrics. Analysis of rainfall structure metrics reveals that spatial and temporal coefficients of variation consistently  
24 correlate with impact severity. Building on these relationships, we propose the Storm Variability Diagram, which  
25 classifies equiprobable events by expected impact and significantly reduces uncertainty in hazard mapping through  
26 ensemble partitioning.

27 Overall, this study provides a proof-of-concept for impact-oriented uncertainty assessment through a modular and  
28 transferable framework, supporting uncertainty-aware flash flood forecasting.

29

## 30 Highlights

- 31 • A Stochastic Rain-on-Grid framework links rainfall structure to flood impacts
- 32 • Rainfall uncertainty attenuates from catchment to street level model outputs
- 33 • The newly proposed Storm Variability Diagram classifies storms by their potential ground impacts
- 34 • Binary classification of storms may reduce uncertainty in flood hazard nowcasting
- 35 • The framework's predictive capability is verified using observed radar data

36

37 **Keywords:** Flash Floods, Rain-on-Grid modelling, Hazard Assessment, Rainfall Uncertainty

## 38 1. Introduction

39 Flash floods are among the most destructive natural hazards globally, causing severe socio-economic and  
40 environmental losses due to their rapid onset, high intensity and localized impacts (Marchi et al., 2010; Borga  
41 et al., 2014). These events typically result from convective precipitation systems that deliver intense rainfall  
42 over small, fast-responding catchments (Llasat et al., 2014). Short lead times and complex hydrodynamic  
43 processes make flash floods particularly challenging for forecasting and emergency management.

44 Understanding and predicting flash-flood generation requires explicitly accounting for a chain of interacting  
45 controls. Precipitation, moisture conditions, infiltration capacity, basin morphology, and land use collectively  
46 control how rainfall is transformed into runoff and routed toward downstream receptors.

47 The dominant source of uncertainty in flood forecasting and impact estimation remains the stochastic nature  
48 of rainfall, whose variability in space and time strongly conditions rainfall–runoff models and flood forecasts  
49 (Beven, 2012; Lin et al., 2022; Peleg et al., 2022; Xu et al., 2025a). Multiple studies document the strong  
50 sensitivity of hydrological response to rainfall space–time variability (e.g. Emmanuel et al., 2015; Wright et  
51 al., 2020; Saharia et al., 2021; Amengual et al., 2021; Ziaee and Abedini, 2023; Pan et al., 2024).

52 A focal theme in the literature is the relative importance of temporal versus spatial rainfall structure. Some  
53 studies find that refining temporal resolution exerts a larger effect on peak flows and timing than adding spatial  
54 detail (e.g. Paschalis et al., 2014; Ochoa-Rodriguez et al., 2015; Yang et al., 2016). Conversely, others report  
55 the opposite or a dominant role of spatial heterogeneity under certain conditions (e.g. Bruni et al., 2015;  
56 Cristiano et al. 2017; 2019; Peleg et al., 2017; Zhu et al., 2018; Zhou et al., 2021; Saharia et al., 2021), also  
57 focusing on the effects of moving storms and storm velocity (Nikolopoulos et al., 2014; Perez et al., 2021;  
58 Chen et al., 2023; Perez et al., 2023; Meng et al., 2025). Actually, the effect of rainfall structure on flood  
59 response is not global: it emerges from the interplay between the storm’s spatiotemporal dynamics and the  
60 catchment’s attributes (Zoccatelli et al., 2010; Emmanuel et al., 2012).

61 One of the main catchment characteristics that significantly affects the flood response is the urban environment,  
62 which adds further complexity. Urbanisation increases impervious areas, introduces engineered drainage  
63 pathways, and alters local atmospheric conditions, magnifying sensitivity to sub-kilometre rainfall  
64 heterogeneity (Cristiano et al., 2017; Yang et al., 2019; Chen et al., 2022). In urban flood studies and modern  
65 flood risk management, the relevant metrics are increasingly focused on hydrodynamic consequences and

66 impact-based (inundation extent, water depth, flow velocity, and derived hazard indices) rather than purely  
67 hydrological (e.g. peak discharge or runoff hydrograph). This transition, emphasised also in international  
68 guidelines (e.g. WMO, 2021), reflects the operational need to warn about “what the weather will do” rather  
69 than just “what it will be” (Kaltenberger et al., 2020; Apel et al., 2022; Costabile et al., 2023; de Moraes 2023;  
70 Mosimann et al., 2024).

71 Nevertheless, much of the current literature has concentrated on catchment-scale hydrological outputs using  
72 lumped or semi-distributed models, which cannot represent localized ground-level impacts that determine  
73 exposure and vulnerability (Khosh Bin Ghomash et al., 2022). This separation between rural hydrological  
74 analyses and urban hydrodynamic impact assessment hinders a comprehensive understanding of flood hazard  
75 variability across coupled rural–urban systems. This limitation is especially pressing in complex settings such  
76 as piedmont regions and urban basins, where bowl-shaped terrain can rapidly channel mountain flood  
77 discharges into densely populated areas, producing flood events that combine both mountain and urban  
78 characteristics (e.g. Bellos et al., 2020; Xu et al., 2025b).

79 Hydrodynamic Rain-on-Grid (RoG) modelling provides a natural pathway to translate high-resolution rainfall  
80 information into localized flood impact assessments. Unlike traditional lumped or semi-distributed approaches,  
81 RoG schemes apply rainfall directly to detailed terrain surfaces and solve water depths and velocities with  
82 two-dimensional shallow water equations solvers. This enables explicit representation of microtopography,  
83 multi-depression storage, and urban flow routing, thereby shifting the focus from bulk hydrologic response to  
84 fine-scale rainfall–topography interactions (Bellos et al., 2025).

85 Advances in computational resources have removed many traditional barriers to hydrodynamic modelling for  
86 nowcasting, enabling large-scale implementation and integration with Numerical Weather Prediction models  
87 (Ming et al., 2020). Concurrently, progress in weather radar technology has yielded spatially and temporally  
88 dense rainfall fields essential for driving such models. These datasets capture variability at scales critical for  
89 microtopographic runoff generation (Berne et al., 2004; Emmanuel et al., 2012) and have consistently  
90 improved runoff and inundation estimation (i.e. Diakakis et al., 2019; Cao et al., 2023; Bournas and Baltas,  
91 2025).

92 By combining radar-derived high-resolution rainfall with efficient RoG modeling, it is now possible to move  
93 beyond generalized runoff predictions and deliver accurate, spatially explicit assessments of street scale  
94 impact-oriented flood forecasting and nowcasting (Costabile et al., 2023).

95 While high-resolution radar products and RoG modelling enable detailed representation of localized flood  
96 processes, they do not eliminate the intrinsic uncertainty of rainfall itself. Spatial and temporal variability,  
97 storm structure, and measurement limitations can all propagate into large differences in flood hazard estimates.  
98 To explore and handle these uncertainties, stochastic rainfall models may play a key role. These models,  
99 ranging from, the so-called weather generators, random cascade methods, to stochastic storm transposition  
100 approaches (e.g. Bras and Rodríguez-Iturbe, 1985; Burton et al., 2010), aim at the generation of synthetic  
101 rainfall data (realizations) that reproduce the stochastic properties of (fine-scale) rainfall and thus allow  
102 controlled experimentation with alternative storm realizations. In doing so, they provide synthetic rainfall  
103 ensembles that may reveal how different storm structures influence hydrological responses (e.g. Paschalis et  
104 al., 2014; von Ruelle et al., 2014; Benoit, 2018).

105 While stochastic rainfall modelling has achieved methodological maturity and Rain-on-Grid approaches have  
106 demonstrated clear value for flash-flood nowcasting, their integration within impact-based and probabilistic  
107 flood assessment frameworks remains heterogeneous across the literature.

108 Recent studies have addressed flood impacts and associated uncertainties using a wide range of methodological  
109 approaches. These include physically based hydrodynamic models driven by Numerical Weather Prediction  
110 ensembles, scenario-based frameworks for coastal and compound flooding, regional to global impact models  
111 relying on synthetic event libraries, probabilistic damage assessments based on exposure and vulnerability or  
112 fragility functions, some of which explored using machine learning and deep learning techniques (e.g. Agonafir  
113 and Zheng, 2025; Pentakota et al, 2025; Song et al., 2025; Wang et al., 2024; Wu et al., 2025).

114 In this context, the combined use of radar-derived rainfall statistics, stochastic generation of equiprobable  
115 storm realizations, and high-resolution Rain-on-Grid hydrodynamic modelling represents a complementary  
116 pathway for impact-oriented flash flood analysis. This approach enables an explicit propagation of rainfall  
117 space–time uncertainty through the hydrological and hydrodynamic response and supports a probabilistic  
118 interpretation of street-scale, hazard-based impact proxies.

119 This paper introduces a Stochastic Rain-on-Grid framework that leverages the synergy between radar-derived  
120 rainfall statistics, stochastic ensemble generation, and high-resolution hydrodynamic modelling to provide  
121 comprehensive uncertainty quantification for flood impact assessment. With reference to the 2017 Mandra  
122 flash flood (West Attica, Greece) as a test case, for which high-resolution radar observations (200 m in space  
123 and 2 min in time) and prior successful Rain-on-Grid simulations (Costabile et al., 2023) are available, we  
124 generate an ensemble of 100 equiprobable storm realizations statistically consistent with the recorded storm.  
125 This event serves not merely as a test case, but as a typical example of a complex, high-impact flash flood in  
126 small watersheds and piedmont urbanized area. Its characteristics make it an ideal setting to establish our  
127 methodological blueprint and to explore the relationships between rainfall variability and flood impact, that  
128 can guide future multi-event investigations.

129 The study, therefore, uses this event as a paradigm to address the following research questions:

- 130 1. Q1: How do equiprobable rainfall scenarios with different spatial and temporal variability influence  
131 hydrological and hydrodynamic impact indicators? Does variability attenuate or amplify as we move  
132 from the catchment scale to the street scale?
- 133 2. Q2: To what extent can simple rainfall structural metrics explain the resulting variability in flood  
134 impacts, serving as effective proxies for impact severity?
- 135 3. Q3: How can the insights generated by our stochastic Rain-on-Grid framework inform and support the  
136 development of impact-based nowcasting systems?

## 137 2. Methods

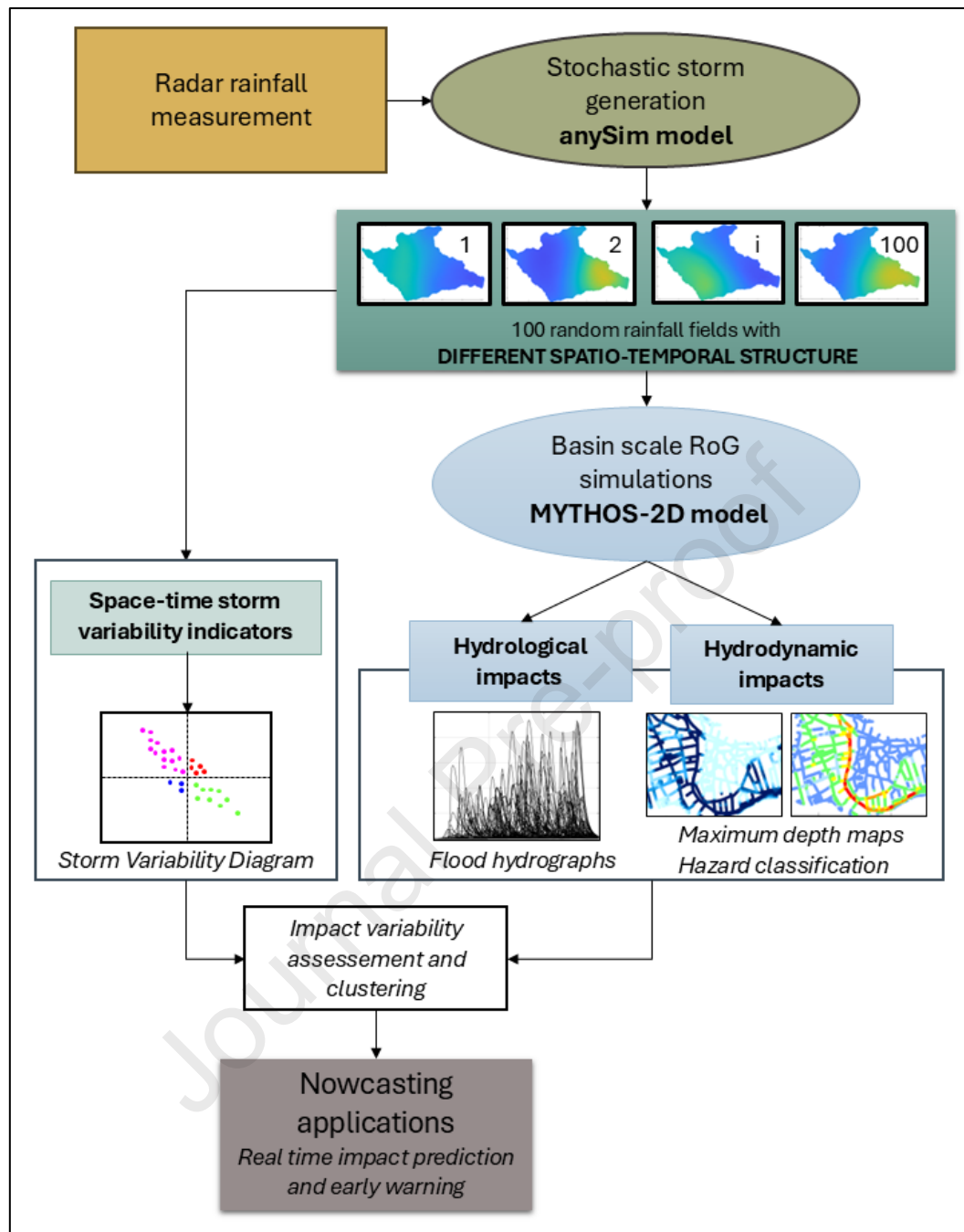
138 The proposed methodological framework presents an integrated approach that combines stochastic rainstorm  
139 generation with RoG modelling for a probabilistic assessment of flood impacts (Figure 1).

140 Radar-based rainfall observations serve as the reference dataset for the stochastic storm generator. This module  
141 is used to produce an ensemble of synthetic rainfall fields (100 in this work) characterized by different spatio-  
142 temporal structures while maintaining statistical consistency with the observed reference event. The generated  
143 precipitation fields constitute the distributed meteorological forcing for RoG model based on the two-  
144 dimensional shallow water equations (2D SWEs), which has been previously calibrated over the target

145 catchment and validated using historical watermarks. This modeling approach simultaneously enables an  
146 investigation at two distinct spatial scales: (i) the catchment scale, where the focus is on determining the  
147 hydrological response, specifically, assessing the hydrological impact in terms of peak discharge and flood  
148 volume, and (ii) the street scale, where the objective is to evaluate the hydrodynamic impacts in terms of  
149 maximum water levels within the urban area and the associated street-scale hazard.

150 Concurrently, a comprehensive analysis of the spatio-temporal variability of the synthetic events is performed  
151 using established indicators from the literature, in order to explore correlations between rainfall properties and  
152 resulting impacts. This approach allows for the classification of events according to their spatio-temporal  
153 patterns and the severity of associated ground impacts.

154 Each module and methodological phase of the framework will be described in detail in the following sections.



155

156

Figure 1. Methodological framework

## 157 2.1 Generation of Synthetic rainfall events: anySim model

158 For the generation of synthetic data numerous approaches have been proposed, often called “weather  
 159 generators” (Wilks and Wilby 1999). For instance, the literature offers ARMA-type models (e.g., Bras and  
 160 Rodríguez-Iturbe 1985; Koutsoyiannis 1999, 2016), point process models (e.g., Onof et al. 2000; Gyasi-Agyei  
 161 2005; Kilsby et al. 2007; Tarpanelli et al. 2012; Kossieris et al. 2016), two-part (discrete - continuous) models,

162 based on Markov chains (e.g., Breinl et al. 2013; Ailliot et al. 2015), resampling methods (e.g., Rajagopalan  
 163 and Lall 1999; Mehrotra et al. 2006) and the more recently-emerged copula-based approaches (e.g., Nelsen  
 164 2007; Bárdossy and Pegram 2009; Serinaldi 2009; Lee and Salas 2011; Tsoukalas et al. 2018a, b, 2019, 2020).  
 165 In this study the stochastically-generated rainfall data were generated using the anySim model, described in  
 166 Tsoukalas et al., (2018b, 2019, 2020), and implemented in R language. anySim allows the simulation of  
 167 stationary non-Gaussian (and intermittent) stochastic processes and random fields with arbitrary, valid (i.e.,  
 168 positive definite), spatiotemporal correlation structures. As a side note, it is remarked that since this study  
 169 focuses on a particular extreme rainfall event (2017 event of Mandra), the implied assumption of stationarity  
 170 is regarded realistic (Koutsoyiannis and Montanari, 2015) and proves particularly useful for the development  
 171 of a parsimonious stochastic modelling approach (i.e., avoid over-parameterization).

172 Therefore, the synthetic data generated represent stochastically-equiprobable events of the historical rainfall  
 173 data, in terms of marginal distribution and spatiotemporal correlation structure, assuming stationarity (within  
 174 the event), while potential advection effects of the rainfall event were not taken into account, which nonetheless  
 175 is arguably difficult to quantify using solely a single rainfall event (or in general, limited historical data).

176 In more detail, using the historical data (as calibration/training data for the stochastic model) provided by the  
 177 National Observatory of Athens (NOA) over the polygon of the study area (Section 3), an ensemble (consisted  
 178 of 100 members) of spatiotemporal rainfall events (realizations of a random field) was generated assuming  
 179 that a process modelled by: 1) a zero-inflated (to account for rainfall intermittency) exponentiated Weibull  
 180 (eWei) distribution (Choudhury 2005), fitted using the method of L-moments (Hosking 1990), 2) a separable  
 181 spatiotemporal correlation structure, provided by the product of a power-exponential (for space) and a Cauchy-  
 182 type (for time) correlation structure (Koutsoyiannis 2000; Tsoukalas et al. 2020). The eWei distribution  
 183 parameters were estimated as follows (using the same notation with the above work):  $\sigma = 2.886$ ,  $a = 3.333$ ,  
 184 and  $\theta = 0.090$ . On the other hand, the product-type spatiotemporal correlation structure was established by of  
 185 the following functions:

186 time – Cauchy-type correlation structure:  $\rho_T(t, \lambda_T = 0.809 \text{ s}, a_T = 0.134) = (1 + \lambda_T a_T t)^{-\frac{1}{a_T}}$   
 187 (1)

188 space – power-exponential:  $\rho_S(d, \lambda_S = 3400.91 \text{ m}, a_S = 1.67) = \exp\left(-\left(\frac{d}{\lambda_S}\right)^{a_S}\right)$  (2)

189 In the above formulas,  $t$ , denotes the temporal lag,  $d$  the Euclidean (separation) distance among two points in  
190 space,  $\lambda_T > 0$  and  $a_T > 0$  are scale and shape (smoothness) parameters, while  $\lambda_S > 0$  and  $a_S \in (0,2)$  are also  
191 scale and shape parameters.  $\lambda_T$  and  $\lambda_S$  are expressed in seconds and meters, respectively.

192 It is noted that all synthetic rainfall fields/events of the ensemble have the same temporal and spatial resolution  
193 (2 min and 200 m), as well as duration (2017-11-14 23.00 GMT until 2017-11-15 11.58 GMT) and spatial  
194 extent with the historical data/rainfall event and the model domain of the area of interest respectively (Section  
195 3).

196 It is important to stress that radar observations and their statistical properties are used in this study solely to  
197 condition and calibrate the stochastic rainfall generator. The generated rainfall fields are not intended to predict  
198 the future evolution of the meteorological system or the occurrence of extreme precipitation events. Instead,  
199 they represent alternative, statistically plausible realizations of the internal space–time variability of the  
200 observed storm. The ensemble of synthetic rainfall events should be interpreted as a sampling of rainfall  
201 structural uncertainty, rather than as a set of forecast scenarios. Each realization is equally probable and  
202 statistically consistent with the observed storm characteristics, and the ensemble is used to explore how this  
203 uncertainty propagates through the hydrological and hydrodynamic models.

204 The choice of 100 realizations reflects a balance between statistical representativeness and computational  
205 feasibility, consistent with the exploratory nature of this study. The ensemble size is not intended to provide an  
206 exhaustive sampling of all possible rainfall configurations, but to allow a statistically meaningful exploration  
207 of the variability of hydrological and hydrodynamic responses induced by rainfall uncertainty.

## 208 **2.2 Rain-on-Grid Modelling**

209 The RoG or Direct Rainfall Method is a modelling strategy of growing importance in both research and  
210 practice. Its main advantage lies in unifying hydrological and hydrodynamic flash flood processes within a  
211 single 2D hydrodynamic model, thus avoiding the need for separate, coupled modelling systems. The  
212 framework operates by applying rainfall forcing directly onto each cell of the computational domain. The  
213 model then simulates surface runoff generation, accounting for infiltration losses (typically through a  
214 Hortonian process), and routes the flow using the 2D SWEs. Other processes, such as evaporation and  
215 groundwater flow, are generally not included, as their influence is considered to be minimal during the rapid

216 timescale of flash flood events. Over the last decade, several RoG models have been developed, and a wide  
217 range of rainfall-runoff processes in small to medium watersheds have been successfully simulated in the  
218 literature (e.g., Costabile et al., 2013; Cea and Bladé, 2015; Fernández-Pato et al., 2016; Bellos and Tsakiris,  
219 2016; Xia et al., 2019; Kirstetter et al., 2021; Buttinger-Kreuzhuber et al., 2022; Caviedes-Voullième et al.,  
220 2023; Cea et al., 2024; Khosh Bin Ghomash et al., 2025; Wang et al., 2025). The popularity of RoG is further  
221 highlighted by its adoption into widely used hydraulic modelling software such as HEC-RAS, TUFLOW and  
222 TELEMAC 2D, for which numerous applications can be found in the literature (Costabile et al., 2021;  
223 Macchione and Lombardo, 2021; Godara et al. 2024; Ennouini et al., 2024; Varra et al., 2025).  
224 The simulator used in the present work is MYTHOS-2D (Modular sYsTem for Hydrodynamic-based rainfall-  
225 runOff Simulations), formerly known as the UniCal model, which was developed at the University of Calabria  
226 (Italy) for research purposes. It solves the 2D-SWE using the Finite Volume Method and it is first order accurate  
227 in time and space. The model includes a dedicated infiltration module, which is based on the well-known  
228 Green–Ampt method, and the friction module based on the use of the Manning-Strickler formulation. The  
229 numerical model, written in Fortran 90, is configured for parallel execution using Message Passing Interface  
230 (MPI), making it suitable for high-performance computing systems. MYTHOS-2D has been proven to provide  
231 reliable results for flood inundation in idealized and real-world urban environments, pluvial flooding in urban  
232 catchments, rainfall–runoff simulations at the basin scale, and flow propagation on infiltrating surfaces  
233 (Costabile et al. 2021; 2024; 2026). All the details are included in the references mentioned above.

### 234 **2.3 Characterization of storm structure using spatio-temporal variability indicators**

235 For each simulated storm scenario, a set of indicators was computed to describe the spatio-temporal  
236 organization of precipitation. These indicators are grouped into two main categories: (i) metrics that describe  
237 the intrinsic spatial and temporal structure of the storm, independently of the catchment geometry, and (ii)  
238 metrics that explicitly account for the spatial distribution of rainfall relative to the morphology of the  
239 catchment.

240 The first group includes three indicators which have been inspired by the framework proposed by Tarasova et  
241 al. (2020), Aala et al. (2025): (i) the temporal coefficient of variation of precipitation rate ( $Tcv$ ), (ii) the ratio

242 between the maximum precipitation rate and the total precipitation volume (*Pratio*), (iii) the spatial coefficient  
 243 of variation of rainfall (*Scv*) during the event.

244 *Tcv* quantifies the variability of catchment-averaged rainfall intensity over time during the storm event (Eq.  
 245 3). This indicator captures how evenly or unevenly rainfall is distributed across time steps.

$$246 \quad T_{CV} = \frac{\sqrt{\text{var}_t(\mathbf{r}_0)}}{\text{mean}_t(\mathbf{r}_0)} \quad (3)$$

247 Where  $\mathbf{r}_0$  represents the vector of the catchment average precipitation during the event, while  $\text{var}_t$  and  $\text{mean}_t$   
 248 are variance and mean operators computed over time.

249 *Pratio* (Eq. 4) distinguishes between intensity-dominated and volume-dominated storms. A higher value  
 250 indicates a short but intense event, while lower values are characteristic of longer, more uniformly distributed  
 251 events.

$$252 \quad Pratio = \frac{\max(\mathbf{r}_0)}{\sum \mathbf{r}_0(t)} \quad (4)$$

253 Where  $r_0(t)$  represents the catchment average precipitation at time  $t$ .

254 *Scv* reported in Eq. 5 and Eq. 6 measures the degree of spatial heterogeneity of precipitation across the  
 255 catchment during the event. It should be emphasized that the index was deliberately weighted by the rainfall  
 256 intensity at time  $t$ , in order to enhance the contribution of more intense precipitation events in the spatial  
 257 characterization. This weighting strategy also mitigates the influence of noise potentially introduced by  
 258 isolated high-intensity pixels during periods of negligible overall precipitation. Higher values indicate more  
 259 localized precipitation patterns, while lower values correspond to more spatially uniform storms.

$$260 \quad S_{CV} = \frac{\sum \mathbf{r}_0(t) \cdot Scv(t)}{\sum \mathbf{r}_0(t)} \quad , \quad Scv(t) = \frac{\sqrt{\text{var}_{xy}(\mathbf{r}(t))}}{\text{mean}_{xy}(\mathbf{r}(t))}; \quad (5,6)$$

261 Where  $\mathbf{r}(t)$  represents the map of precipitation rate at time  $t$ , while  $\text{var}_{xy}$  and  $\text{mean}_{xy}$  represent variance and  
 262 mean operators computed across space.

263 While the first group of indicators describes the intrinsic organization of the rainfall event independently of its  
 264 position within the catchment, the second group relates storm spatial patterns to catchment morphology,  
 265 following the framework by Zoccatelli et al. (2011). Specifically, the first ( $\Delta_1$ ) and second ( $\Delta_2$ ) scaled moments  
 266 of rainfall are computed:  $\Delta_1$  quantifies the relative position of the rainfall centroid with respect to the outlet  
 267 (Eq. 7), with values  $>1$  indicating upstream concentration and  $<1$  indicating downstream concentration;  $\Delta_2$   
 268 measures the spatial spread of rainfall along the main flow path (Eq. 7), where values  $>1$  suggest multimodal  
 269 distributions,  $<1$  indicate compact storms, and  $\sim 1$  corresponds to uniform patterns.

$$270 \quad \Delta_1 = \frac{PR_1}{R_0 g_1} \quad (7)$$

$$271 \quad \Delta_2 = \frac{1}{g_2 - g_1^2} \left[ \frac{R_2}{R_0} - \left( \frac{R_1}{R_0} \right)^2 \right] \quad (8)$$

272 Where  $R_n$  represents the  $n$ -th spatial moment of catchment rainfall while  $g_n$  represents the  $n$ -th moment of the  
 273 flow distance, i.e. the distance along the runoff flow path from a given point to the outlet.

274 Details about the interpretation and expected ranges of these indicators are summarized in prior works (e.g.,  
 275 Zoccatelli et al., 2011; Tarasova et al., 2020; Aala et al., 2025).

## 276 2.4 Impact Metrics

277 In order to quantify the severity of ground-level impacts associated with the ensemble of storm events, a  
 278 distinction is made between the watershed scale, in terms of hydrological response, and the street scale focusing  
 279 on the hydrodynamic impact.

280 The hydrological response is evaluated through the analysis of the shape of simulated flood hydrographs  
 281 resulting from each storm event. Specifically, for each discharge hydrograph three key metrics are extracted: (i)  
 282 total surface runoff volume, (ii) peak discharge, and (iii) time to peak. These metrics are calculated at selected  
 283 cross-sections located upstream of the urban area of interest.

284 Conversely, the hydrodynamic impact is assessed exclusively within the urban domain, in terms of:

285 (i) maps of maximum water depth, (ii) inundation extent which was computed as the sum of the cell areas with  
 286 maximum flow depth above 0.10 m, and (iii) maps of hazard classification.

287 The latter are derived using the Generalized Flood Impact Index developed by the Australian Institute for  
 288 Disaster Resilience (AIDR, 2017). This index defines six hazard categories based on threshold values of water  
 289 depth  $h$ , and the product of water depth and flow velocity  $h \cdot v$ , as detailed in Figure 2.  
 290 This index is a useful metric for identifying the impacts of flooding on people, vehicles, and buildings, and it  
 291 also provides a practical way to account for uncertainties in the simulated flood variables (i.e., water depths and  
 292 flow velocities) by transforming them into six hazard classes (Bellos et al., 2025). These hazard classes should  
 293 be interpreted as hazard-based impact proxies derived from physically simulated flood characteristics, rather  
 294 than as direct estimates of exposure- or vulnerability-dependent outcomes such as the number of affected people  
 295 or economic losses. More detailed impact assessments, including the estimation of building damage or economic  
 296 losses, would require the coupling of flood hazard outputs with exposure data and vulnerability or fragility  
 297 curves for the affected elements. While such approaches are well established in the literature, they are beyond  
 298 the scope of the present study, which deliberately focuses on the probabilistic characterization of hazard-based  
 299 impact proxies. In this respect, the adopted index provides an operationally meaningful characterization of flood  
 300 hazard severity that represents a necessary upstream component of impact-based forecasting and disaster risk  
 301 reduction frameworks, upon which population exposure, vulnerability, and damage models can subsequently be  
 302 applied, and it is particularly well suited for operational use by civil protection services, as it can be  
 303 communicated more easily to the vulnerable population.

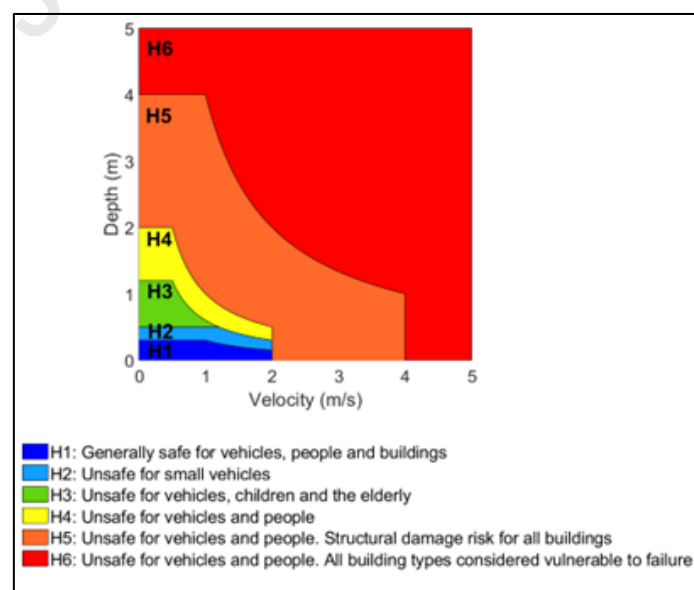


Figure 2. Hazard categories according to the AIDR (2017)

### 306 3. Case study and model settings

307 The flood event occurred on 15 November 2017 in the town of Mandra, located about 30 km west of central  
308 Athens (Greece), in the western part of the greater Athens metropolitan area (Figure 3). It was one of the most  
309 catastrophic flood events in Greece in the last 40 years, resulting in the loss of 24 lives and causing extensive  
310 damage to Mandra's infrastructure. Mandra is situated at the outlet of two small to medium-sized catchments  
311 (approximately 20–25 km<sup>2</sup> each), drained by the Agia Aikaterini and Soures streams. The storm which flooded  
312 Mandra was highly localized and therefore, there were no ground observations at the neighboring  
313 meteorological stations. Stamou (2018) and Mitsopoulos et al. (2022) estimate that the rainfall event had a  
314 return period of 150 to 200 years. Moreover, Ntigliakakis et al. (2018) estimated the return period of the event,  
315 through a reverse engineering approach. They found that for rainfall time scales which vary from 3 h to 6 h,  
316 the return period of the storm lies within the range of 100-200 years. The Agia Aikaterini stream is integrated  
317 into the town's urban drainage system. Across the entire computational domain, the soil is classified as loam.  
318 The spatial and temporal characteristics of the storm were captured by NOA's XPOL, an X-band dual-  
319 polarization Doppler weather radar, with spatial and temporal resolutions of 200 m and 2 min, respectively.  
320 This mobile radar is typically installed on a 500 m-high hill in the northern suburbs of Athens and operates  
321 during rainfall events affecting the wider Athens area (see, e.g. Kalogiros et al., 2013).

322 The storm was highly localized as a result of an orographic phenomenon driven by Mount Pateras, which lies  
323 upstream of the catchments. At that time, Greece did not have an impact-based early warning system; only  
324 qualitative weather-related warnings were issued by the meteorological service. In this case, even numerical  
325 weather models failed to capture the event, while ground-based meteorological stations recorded only small  
326 rainfall amounts, as they were located far from the storm center.

327 For all the simulated scenarios, MYTHOS-2D was run using the same settings as in a previous study (Costabile  
328 et al., 2023). In that work, it was demonstrated that MYTHOS-2D, when coupled with radar data, was able to  
329 provide accurate predictions of the flooded area extent and even reproduce the water marks observed during  
330 post-event surveys at more than 30 locations within the town of Mandra. For completeness, some information  
331 about the model setup is reported here.

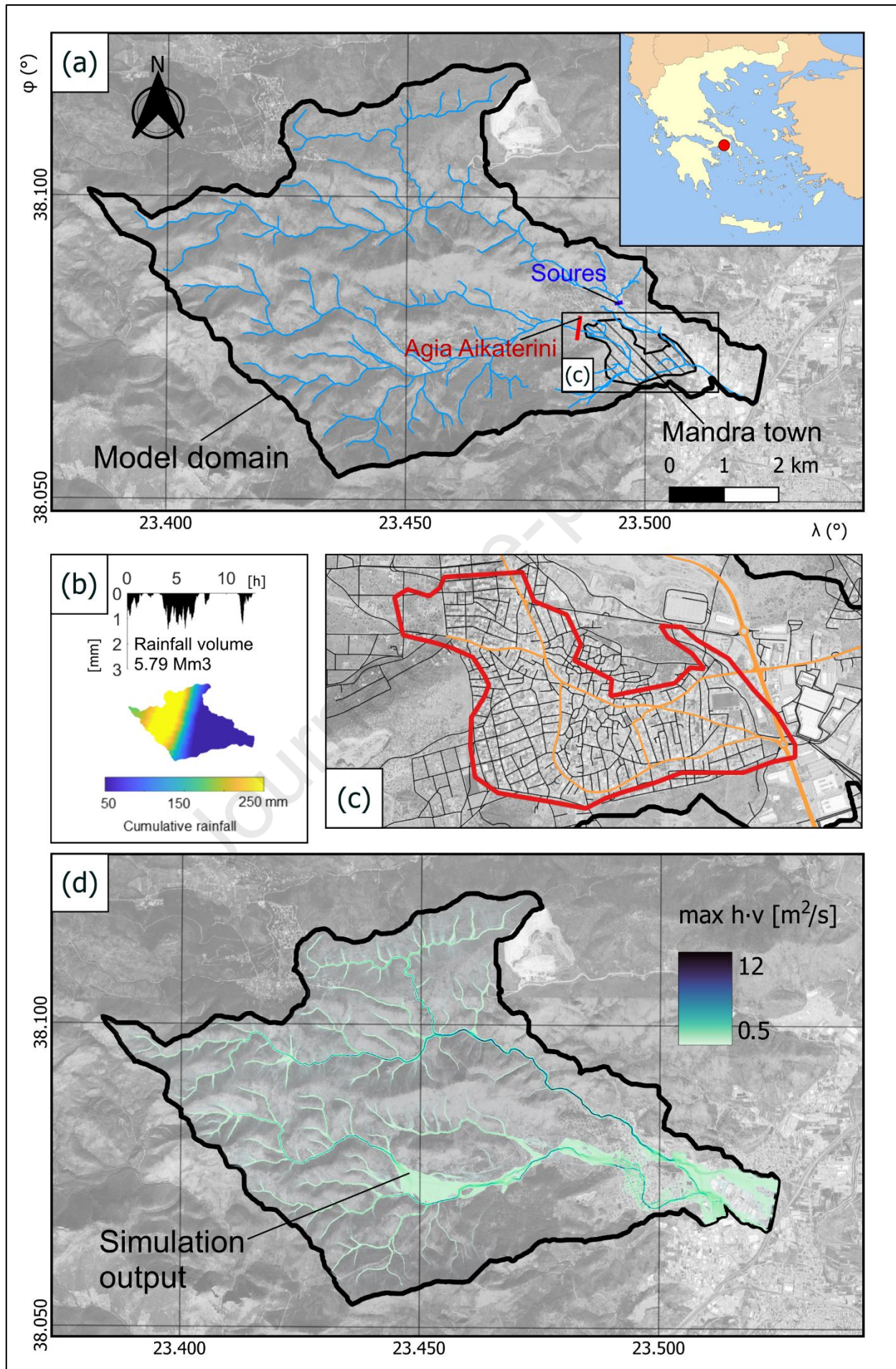
332 The computational domain is based on an unstructured grid composed of triangular irregular elements of  
333 varying size. Specifically, a coarse resolution was adopted for hillslopes (50–60 m<sup>2</sup>), a more refined grid for  
334 the channel network and floodplain (20–30 m<sup>2</sup>), and a finer resolution within the town (up to 9 m<sup>2</sup>) to  
335 adequately capture flow dynamics through buildings and streets. Overall, the grid consists of approximately  
336 10<sup>6</sup> computational elements.

337 Buildings were represented using the “building hole” approach, by applying appropriate solid-wall boundary  
338 conditions. For the domain boundaries, transmissive (open) conditions were imposed at the most downstream  
339 section, while solid-wall conditions were applied along the catchment boundaries. Furthermore, following  
340 Bellos et al. (2020), three roughness classes were adopted across the domain, while a single class corresponding  
341 to loam was assumed and uniformly distributed across the two watersheds. Further details and the specific  
342 values of the calibrated parameters can be found in our previous work (Costabile et al., 2023).

343 Flood maps were computed for the entire catchment (see Figure 3, bottom), but for impact analysis purposes  
344 we focus hereafter only on the town of Mandra.

345

346



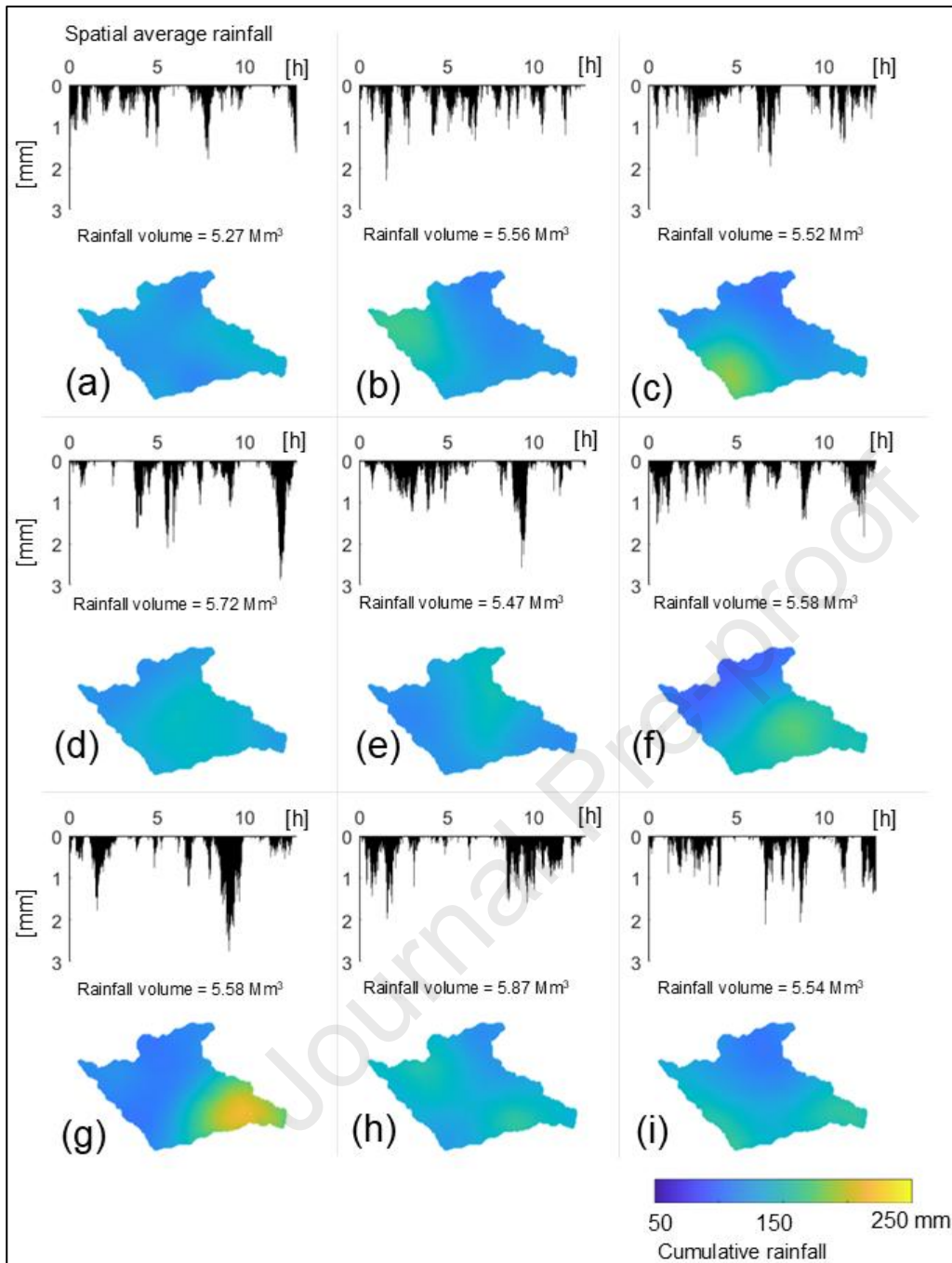
348 **Figure 3.** Application area of the RoG model, location of the hydrograph calculation sections, and position of the urban  
349 center of Mandra (a). Rainfall patterns for the recorded event. Catchment average rainfall time series ( $\Delta t = 2$  min) (top),  
350 spatial cumulative (bottom) and indication of the total rainfall volume (b). Details of the main road network within the  
351 town of Mandra (c). Example of max depth  $\cdot$  velocity map extended to the entire study area (d).

## 352 4. Results

### 353 4.1 Variety of generated spatial-temporal rainfall structures by AnySim

354 The ensemble of 100 stochastic scenarios generated by the anySim model displays a wide range of spatial and  
355 temporal patterns. Figure 4 shows a selection of representative cases, highlighting the diversity of space-time  
356 rainfall structures within the ensemble. Spatial heterogeneity is illustrated through cumulative rainfall maps,  
357 which emphasize differences in the spatial distribution of total precipitation volumes across the catchment.  
358 Temporal variability is depicted by the spatially averaged rainfall time series ( $\Delta t = 2$  minutes), providing insight  
359 into the timing and intensity of rainfall events. Focusing on the spatial distribution, Fig. 4(a) shows a relatively  
360 uniform pattern, especially when compared to panels (b) and (c), which display a concentration of cumulative  
361 rainfall in the upstream areas, or panels (d) and (e), where rainfall volumes are predominantly concentrated in  
362 the central region. A different pattern emerges in panels (f) and (g), which show a clear concentration of rainfall  
363 downstream, while panels (h) and (i) reveal multiple localized rainfall cores. A certain degree of variability  
364 also emerges from the time series, which illustrate different scenarios: peak intensities occurring at the  
365 beginning of the event (b), at the end (d), more temporally uniform rainfall (f), or rainfall distributed across  
366 different moments in time (h).

367



369

370 **Figure 4.** Representative examples of the spatial and temporal variability observed within the ensemble of 100 stochastic  
 371 rainfall scenarios generated by anySim. Each panel (a–i) shows the catchment average rainfall time series ( $\Delta t = 2$  min)  
 372 (top), the corresponding spatial cumulative (bottom), and an indication of the total rainfall volume for the selected  
 373 scenario. The spatial maps highlight a wide range of rainfall patterns, from more uniform distributions (a), to localized  
 374 accumulations in the upstream (b, c), centre (d, e), downstream (f, g), or in multiple locations (h, i). The rainfall time  
 375 series reveal different temporal dynamics, including events with early (b) or late (d) intensity peaks, more temporally  
 376 uniform rainfall (f), or concentration at varying times (h). Although the spatial structure varies considerably, total  
 377 precipitation remains within  $\sim 10\%$  of the ensemble mean, with the historical event closely matching it.

378 The total precipitation across the 100 stochastic scenarios differs by a maximum of  $\pm 8\%$  from the ensemble  
379 mean, with only one outlier showing a deviation of  $-12\%$ . The real event, evaluated over the same temporal  
380 window, yields a total volume of  $5.79 \text{ Mm}^3$ , while the stochastic ensemble has an average of  $5.72 \text{ Mm}^3$ , a  
381 coefficient of variation (CV) of  $5\%$  and an interquartile CV ( $Q_{25}-Q_{75}$ ) of  $1\%$ . Therefore, the observed historical  
382 event recorded a total volume which is very close to the ensemble mean.

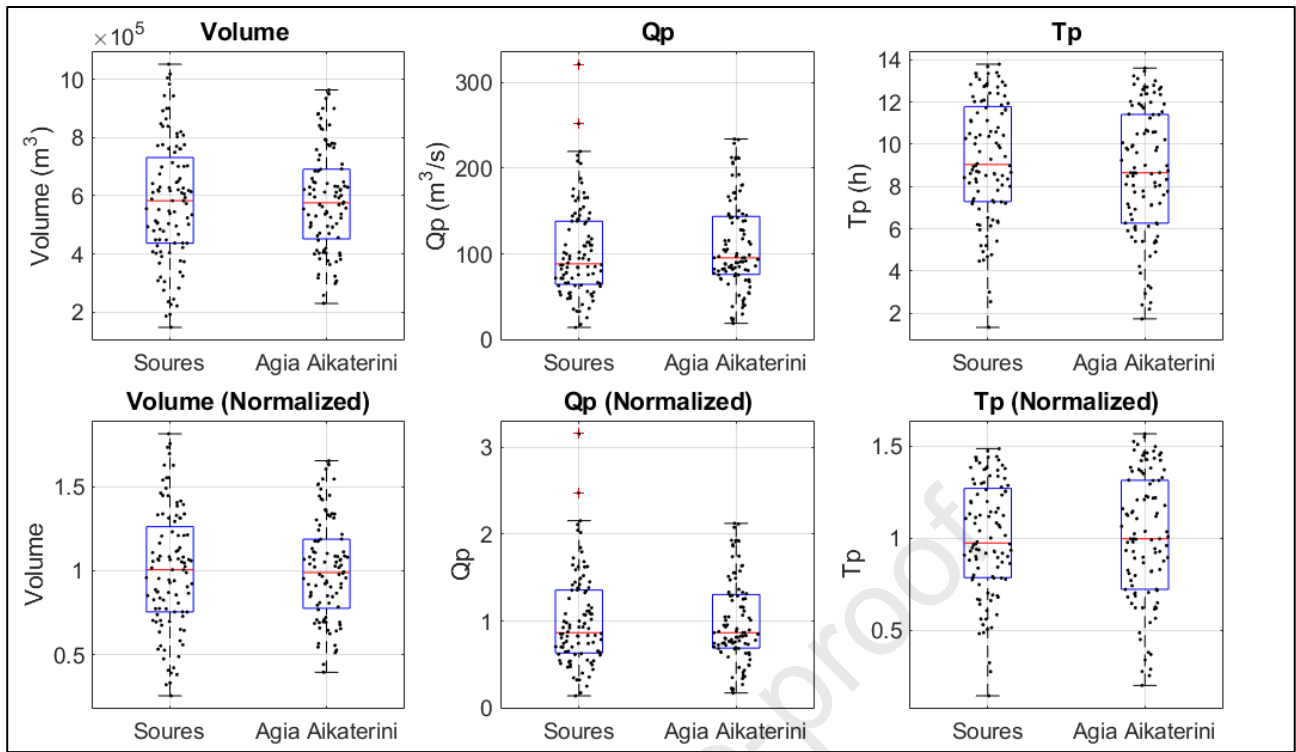
383 This confirms that the ensemble maintains realistic event-integrated rainfall volumes, despite the considerable  
384 variability in space-time patterns.

385

## 386 **4.2 Variability from the catchment scale to the street scale**

### 387 *4.2.1 Variability of hydrological response*

388 The variety in the spatial and temporal structure of the rainfall scenarios translates into a range of hydrological  
389 responses. Figure 5 presents the distributions of surface runoff volume, peak discharge, and time-to-peak for  
390 the hydrographs computed at the Agia Aikaterini and Soures cross sections. Each metric has been standardized  
391 by its respective ensemble mean to facilitate comparison across scenarios. For each plot, the actual ensemble  
392 mean and the coefficient of variation (CV) of the corresponding indicator are also reported in Table 1, providing  
393 insights into the sensitivity of the hydrological response to rainfall variability.



394

395

396

397

**Figure 5.** Boxplots of Volume, Peak Discharge ( $Q_p$ ), and Time to Peak ( $T_p$ ) of the hydrographs simulated for the Soures and Agia Aikaterini streams in correspondence to the cross section located as shown in Fig.2. Simulated values (top) and standardized values with respect to the ensemble mean (bottom).

Section	Ensemble mean			Ensemble CV		
	Volume ( $m^3$ )	$Q_p$ ( $m^3/s$ )	$T_p$ (h)	Volume	$Q_p$	$T_p$
Soures	580158	101.9	9.3	0.38	0.53	0.31
Agia Aikaterini	582955	110.2	8.7	0.31	0.48	0.35

398

399

**Table 1.** Ensemble mean and Coefficient of Variation of Volume, Peak Discharge and Time to peak of the hydrograph simulated at Soures and Agia Aikaterini cross sections.

400

401

402

403

404

405

406

Peak discharge varies from approximately  $14 m^3/s$  to more than  $320 m^3/s$ , while time to peak ranges from just over 1 hour to nearly 14 hours. Similarly, runoff volumes span from about  $148,000 m^3$  to over  $1,050,000 m^3$ . With coefficient of variation ( $CV$ ) reaching up to 0.53 for peak discharge and around 0.35 for time to peak, the high sensitivity of flow dynamics to the spatio-temporal structure of rainfall results evident. However, it is worth noting that the lowest values of peak discharge may be partly explained by rainfall peaks occurring downstream of the cross-sections used to compute discharge (red and blue sections in Figure 3), which makes them less representative of actual hydrological impacts.

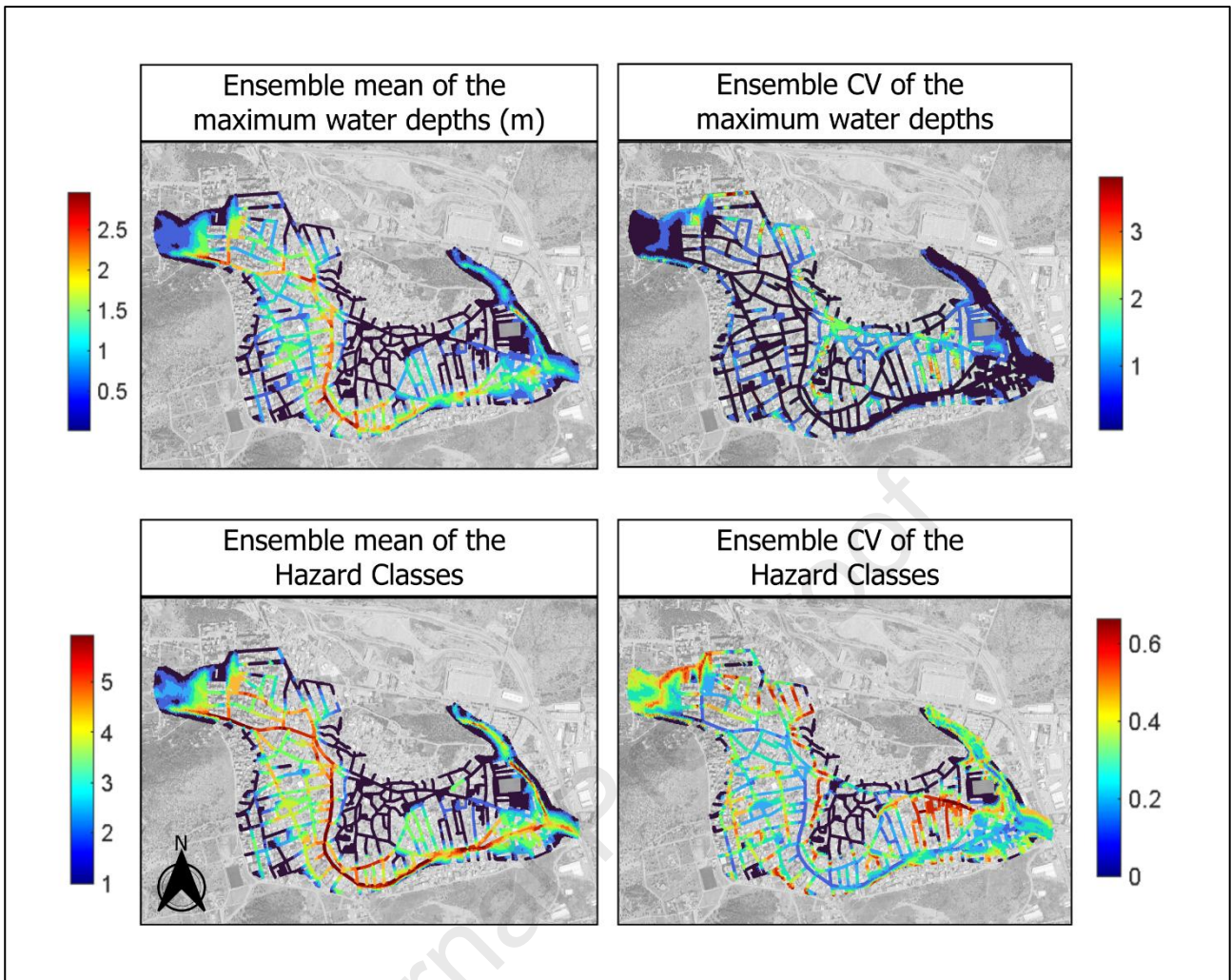
407 *4.2.2 Variability of maximum water depths and hazard classes*

408 Focusing on the urban area, Figure 6 illustrates the ensemble mean (left) and coefficient of variation (right) of  
409 maximum water depth (top) and flood hazard classes derived using the AIDR methodology (bottom). The  
410 mean water depth map highlights critical zones, with localized values exceeding 2.5 m, while the  
411 corresponding hazard classification reveals a concentration of higher-risk streets near the main road, gradually  
412 decreasing toward the periphery.

413 The *CV* provides a complementary perspective, enabling a direct comparison between the continuous variable  
414 (water depth) and the discrete hazard classes. Overall, variability appears moderate ( $CV < 1$ ), though certain  
415 hotspots exhibit high sensitivity ( $CV > 2$ ), reflecting the influence of rainfall variability on flood dynamics.  
416 Mean hazard levels range predominantly from medium to high (classes 3–5), especially along main streets.

417 *CV* values for hazard classes reach up to 0.6 in some locations, indicating areas where even small  
418 hydrodynamic changes may alter the impact classification. In areas experiencing severe flooding, the *CV* of  
419 both variables are comparable. However, in less affected zones, the discretization tends to smooth out  
420 variability, leading to hazard-class *CV* values that can be up to an order of magnitude lower than those  
421 associated with water depths.

422

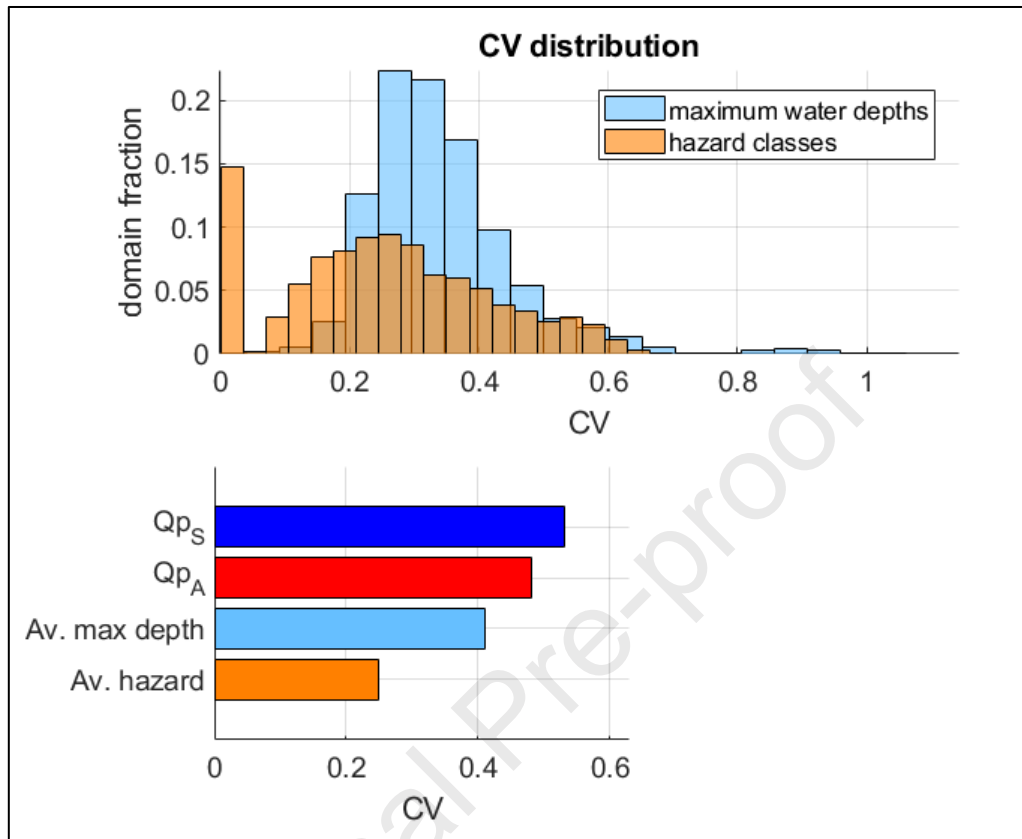


423

424 **Figure 6.** Ensemble mean and coefficient of variation ( $CV$ ) of maximum water depth (top) and flood hazard class  
 425 (bottom) for the urban area of Mandra. Hazard classes are computed based on maximum water depth and velocity  
 426 following the AIDR methodology. Each map uses an independent colour scale.

427 To further characterize these spatial patterns, Figure 7 (top) compares the distribution of  $CV$  values for both  
 428 maximum water depth (considering depths  $> 0.10$  m) and hazard classes. As expected, the continuous variable  
 429 exhibits greater variability, with an average  $CV$  of 0.43 and a wider range, including more frequent occurrences  
 430 of high values. In contrast, the hazard class  $CV$  distribution, averaging 0.25, is narrower and skewed toward  
 431 lower values. This behavior highlights the dampening effect of the hazard mapping process, which reduces  
 432 sensitivity to minor variations in water depth. Overall, the coefficients of variation ( $CV$ s) computed across  
 433 different impact metrics variables reveal a progressive attenuation of variability moving from catchment to  
 434 street level (Figure 7, bottom): while hydrological indicators (e.g., peak discharge) exhibit the highest

435 sensitivity to rainfall structure, this variability is partially dampened in the spatial distribution of maximum  
 436 water depths, and further reduced in the final classification of flood hazard.



437

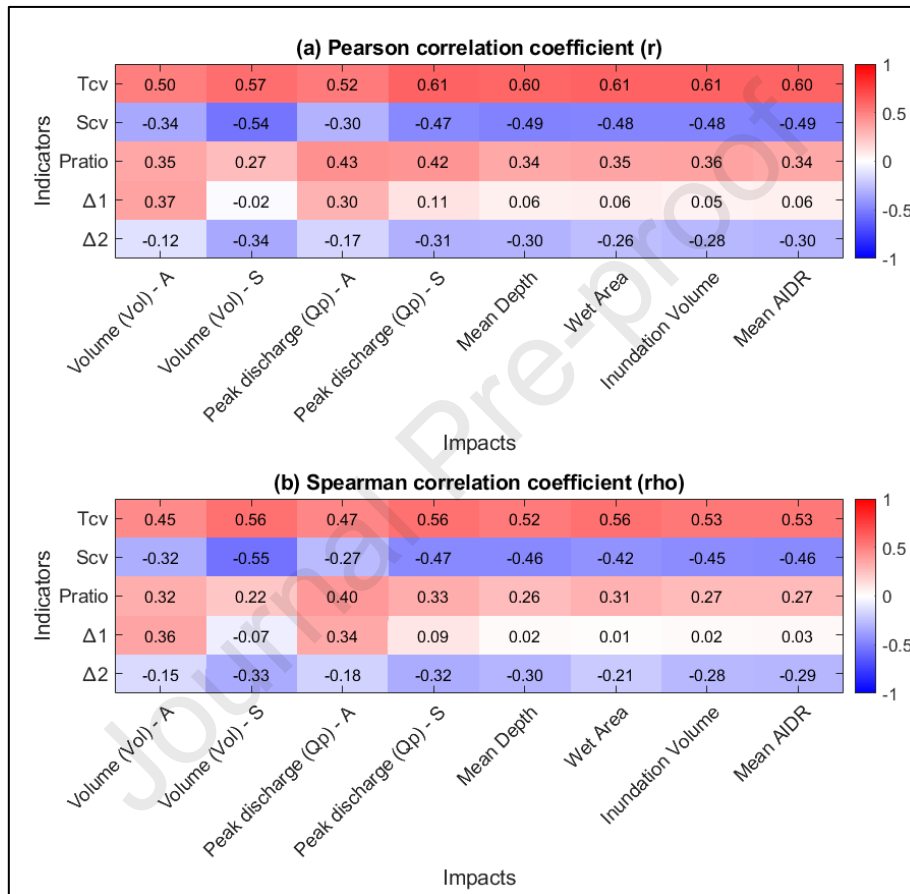
438 **Figure 7.** Comparison of the spatial distribution of CV values for maximum water depths (considering only cells with  
 439 depths > 0.10 m) and hazard classes across the urban domain. The figure also compares the CV values of peak discharges  
 440 simulated at the Soures and Agia Aikaterini cross sections with the average CVs computed for maximum water depths  
 441 and hazard classes.

#### 442 4.3 Rainfall structure metrics as predictors of flood impacts

##### 443 4.3.1 Correlation between rainstorm spatio-temporal structure and flood impacts

444 Given the observed variability in flood impacts, we have explored to what extent this variability is influenced  
 445 by the spatio-temporal structure of rainfall. Figure 8 presents heatmaps of the Pearson (8a) and Spearman (8b)  
 446 correlation coefficients between the rainfall structure indicators introduced in Section 2.3 and the impact

447 metrics described in Section 2.4, computed across the full set of 100 scenarios. The use of a blue-to-red color  
 448 scale helps visually emphasize both the strength and the direction of the correlations.  
 449 Overall, both correlation analyses reveal consistent patterns of association, with only minor differences in  
 450 coefficient magnitude between the two methods. This consistency suggests that the relationships between  
 451 rainfall structure indicators and impact metrics are predominantly linear, although some non-linear trends may  
 452 be better captured by the rank-based Spearman correlation.



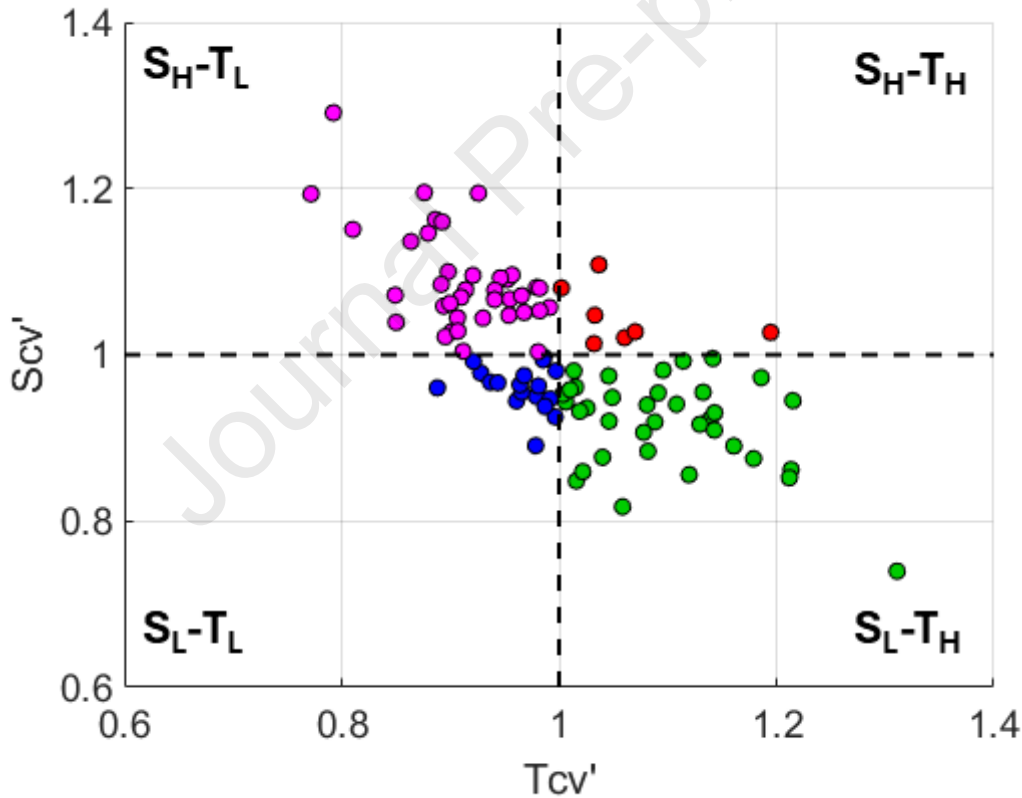
453  
 454 **Figure 8.** (a) Pearson and (b) Spearman correlation coefficients between indicators of rainfall spatio-temporal variability  
 455 ( $T_{cv}$ ,  $Scv$ ,  $Pratio$ ,  $\Delta_1$ ,  $\Delta_2$ ) and impacts in terms of runoff volumes computed at Agia-Aikaterini (A) and Soures (S) cross  
 456 sections, maximum depths (spatial average), inundated areas, inundation volume, AIDR hazard class (spatial average).  
 457 Among the indicators,  $T_{cv}$  shows strong and positive correlations with all impact variables in both Pearson ( $r$   
 458 = 0.50 - 0.61) and Spearman ( $\rho$  = 0.45 - 0.56) analyses, highlighting its robust influence on hydrological  
 459 and hydraulic responses.  $Scv$ , on the other hand, exhibits consistently negative correlations, particularly with  
 460 peak discharge and inundation-related metrics (e.g.,  $\rho$  = -0.55 with peak discharge at Soures), suggesting that  
 461 greater spatial spread in rainfall is associated with lower impact severity.

462 The indicators  $\Delta_1$  and  $\Delta_2$  display weaker and less consistent relationships with the impacts. In particular,  $\Delta_2$   
 463 generally shows low or negative correlations across most metrics, with slightly stronger effects observed in  
 464 the Spearman analysis (e.g.,  $\rho = -0.33$  with inundated area).

465 Overall, the results indicate that  $Tcv$ , and to a lesser extent,  $Scv$ , are the most relevant indicators for explaining  
 466 the variability in flood impacts across the ensemble, underscoring the importance of temporal concentration  
 467 and spatial coherence in driving hydrological response.

#### 468 4.3.2 Storm variability diagram based on the anySim-generated output

469 Given the prominent roles of  $Tcv$  and  $Scv$  in controlling impact variability, we propose a new framework, the  
 470 Storm Variability Diagram, to classify and interpret the joint influence of these two indicators (Figure 9).



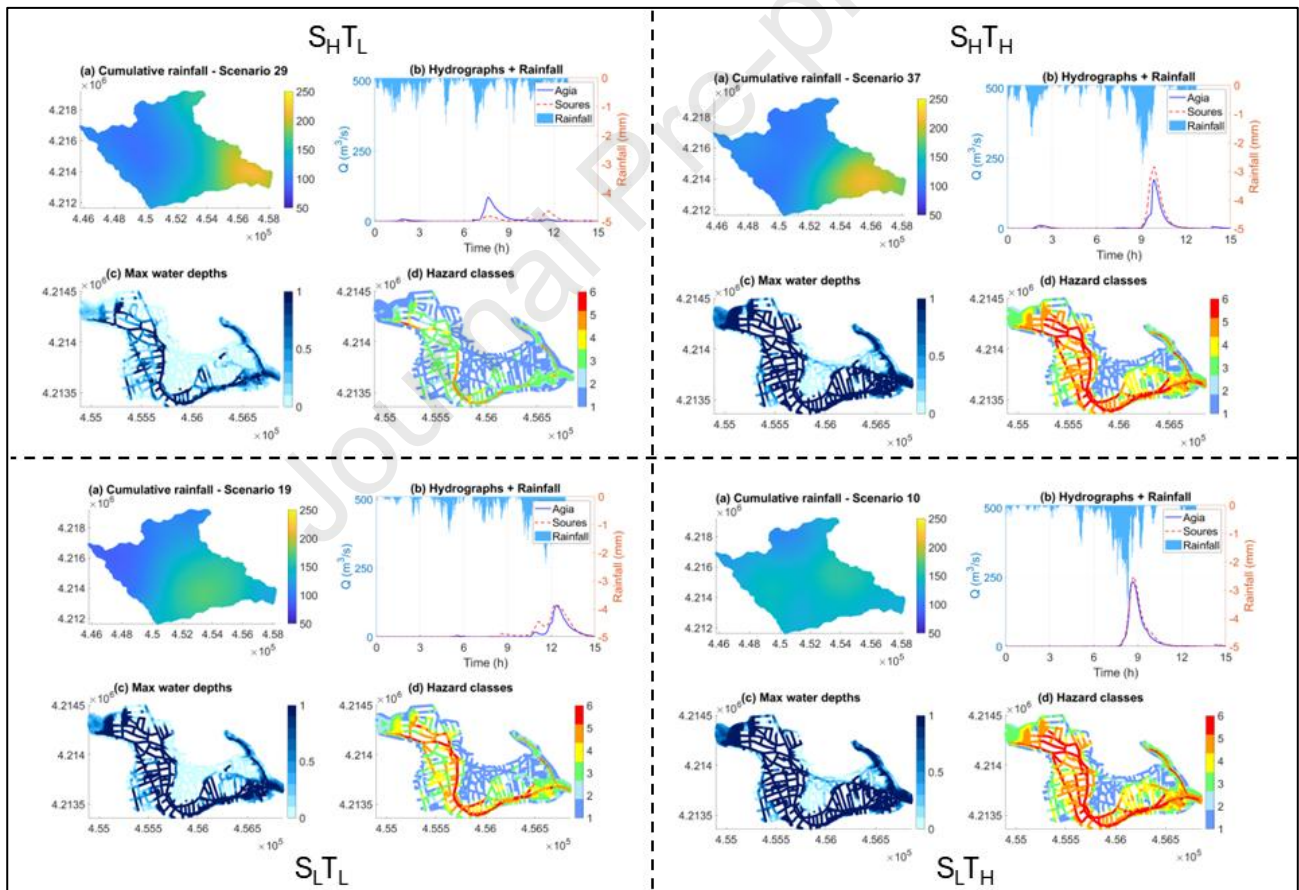
471

472 **Figure 9.** Distribution of the stochastic storms on the Storm Variability Diagram showing the relationship between  $Scv'$   
 473 and  $Tcv'$ , standardized values of  $Scv$  and  $Tcv$  respectively

474 This diagram is a Cartesian plane where the x-axis represents the standardized temporal coefficient of variation  
 475 ( $Tcv'$ ) and the y-axis the standardized spatial coefficient of variation ( $Scv'$ ) of each storm. Standardization is

476 carried out using the ensemble mean as reference, to emphasize storms with  $Scv$  and  $Tcv$  values higher or lower  
 477 than the ensemble mean and facilitate comparison and interpretability.

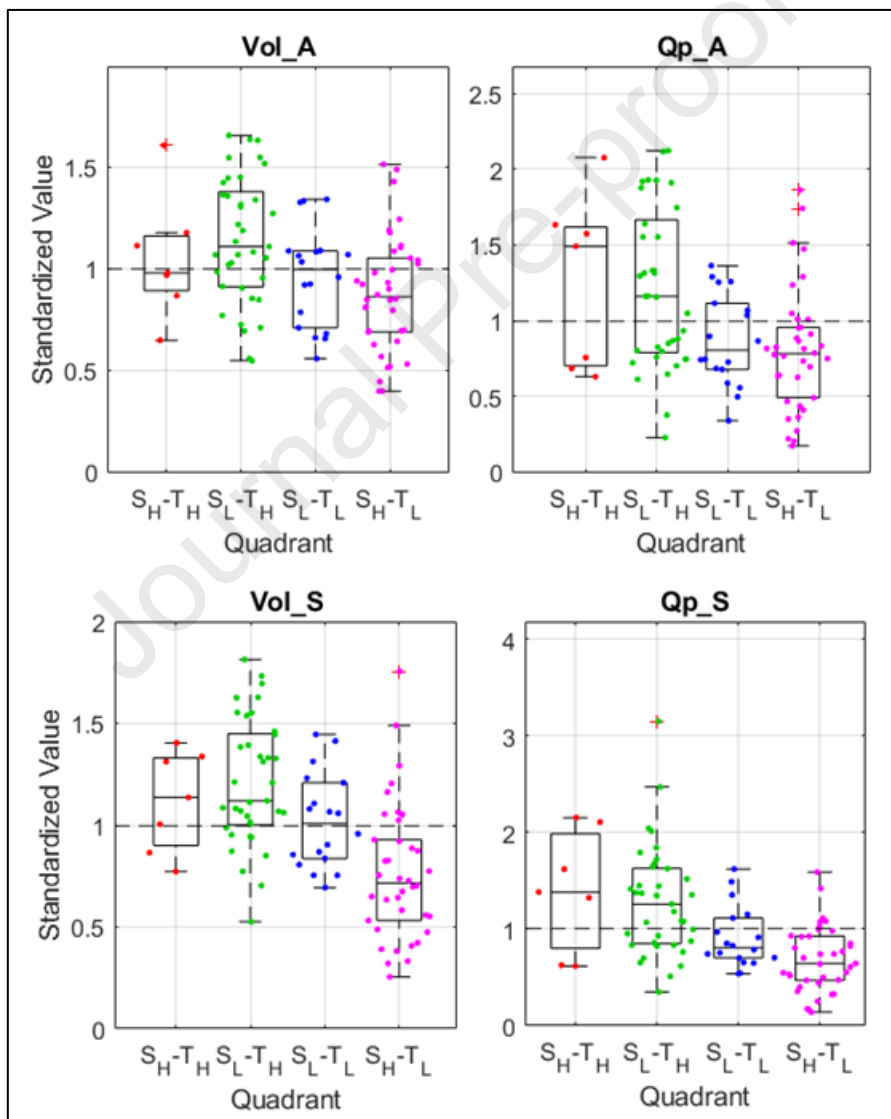
478 The space is divided into four quadrants, according to the combination of higher (H) and lower (L) values of  
 479  $Scv$  and  $Tcv$ . For example,  $S_H-T_H$  is related to higher values of both  $Scv$  and  $Tcv$ , whereas  $S_L-T_L$ , is associated  
 480 to the lower values of both  $Scv$  and  $Tcv$ . Physically, storms in the  $S_H-T_H$  quadrant are characterized by both  
 481 strong temporal fluctuations and high spatial heterogeneity. Figure 9 shows the distribution of the 100  
 482 stochastic rainstorms generated by anySim in the Storm Variability Diagram. Different colours highlight the  
 483 presence of distinct clusters associated with the four quadrants of the diagram. The largest groups correspond  
 484 to storms in the  $S_H-T_L$  (magenta points) and  $S_L-T_H$  (green points) quadrants, while the other two quadrants  
 485 contain fewer events.



486

487 **Figure 10.** Hydrological and hydrodynamic impacts of four representative storm. Each quadrant corresponds to a storm  
 488 type from the Storm Variability Diagram and displays: (a) cumulative rainfall, (b) rainfall hctograph and hydrograph  
 489 simulated at Agia Aikaterini and Soures cross sections, (c) maximum water depths, and (d) hazard classification in the  
 490 Mandra town.

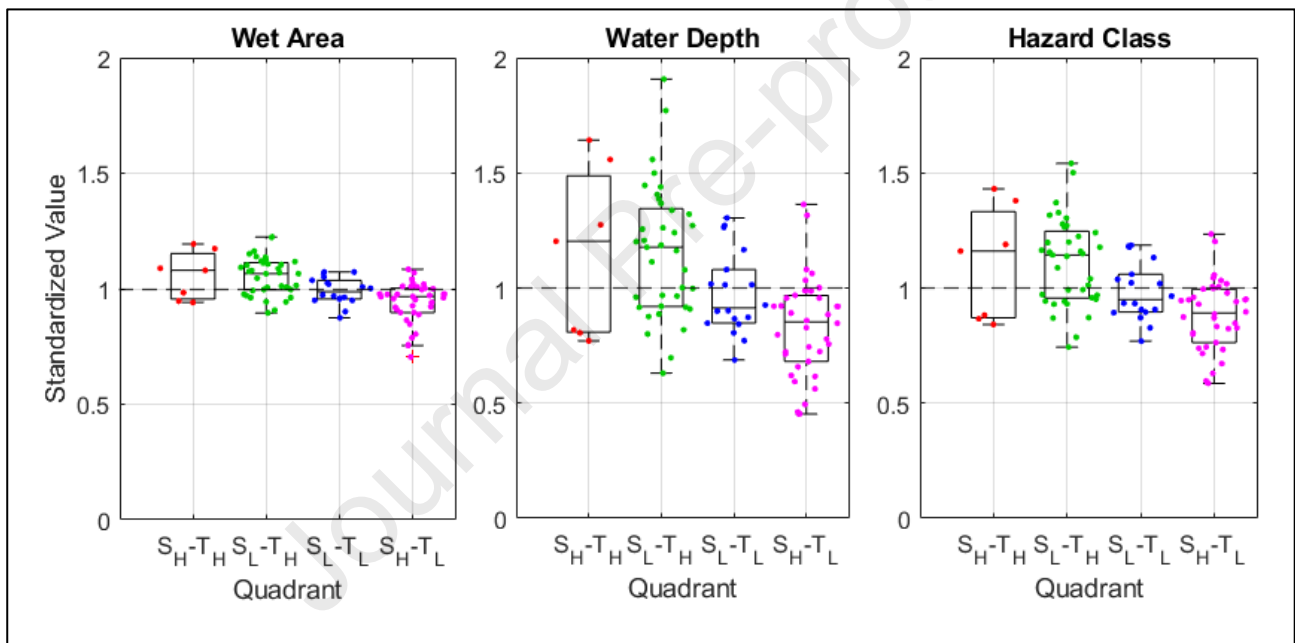
491 Figure 10 illustrates representative scenarios and their associated impacts from each quadrant of the Storm  
 492 Variability Diagram. For each scenario, the following elements are presented: (a) cumulative rainfall  
 493 distribution; (b) time series of spatially averaged rainfall intensity alongside simulated hydrographs at key  
 494 locations; (c) maps of maximum simulated water depths; and (d) final hazard classification maps for the city  
 495 centre of Mandra. The storm depicted in the  $S_H-T_L$  quadrant produces markedly less intense impacts, both in  
 496 terms of simulated hydrographs and in the maps of maximum water depths and hazard classes, compared to  
 497 the other three quadrants, particularly those on the right side of the diagram, corresponding to the higher  
 498 temporal variability ( $T_H$ ) region.



499

500 **Figure 11.** Hydrological impacts: standardized flood volume and peak discharge computed for Agia Aikaterini cross  
 501 section (top), Soures (bottom).

502 The relationship between the quadrants and hydrological impacts is summarized in Figure 11, which presents  
 503 combined boxplots and swarmplots of standardized Volume and Peak Discharge, separated by the four  
 504 quadrants of the Storm Variability Diagram. Results are shown for both the Agia Aikaterini (top) and Soures  
 505 (bottom) catchments. The most severe impacts are associated with storms characterized by low spatial  
 506 variability and high temporal variability ( $S_L-T_H$ ). These trends are similarly reflected in the hydrodynamic  
 507 impacts, which are summarized here in terms of flooded area extent, spatial average of maximum water depths,  
 508 and spatial average of the AIDR hazard class. Figure 12's boxplots highlight a clear pattern of decreasing  
 509 median values and variability when moving from scenarios in the  $S_H-T_H$  quadrant toward those in the  $S_H-T_L$   
 510 quadrant.

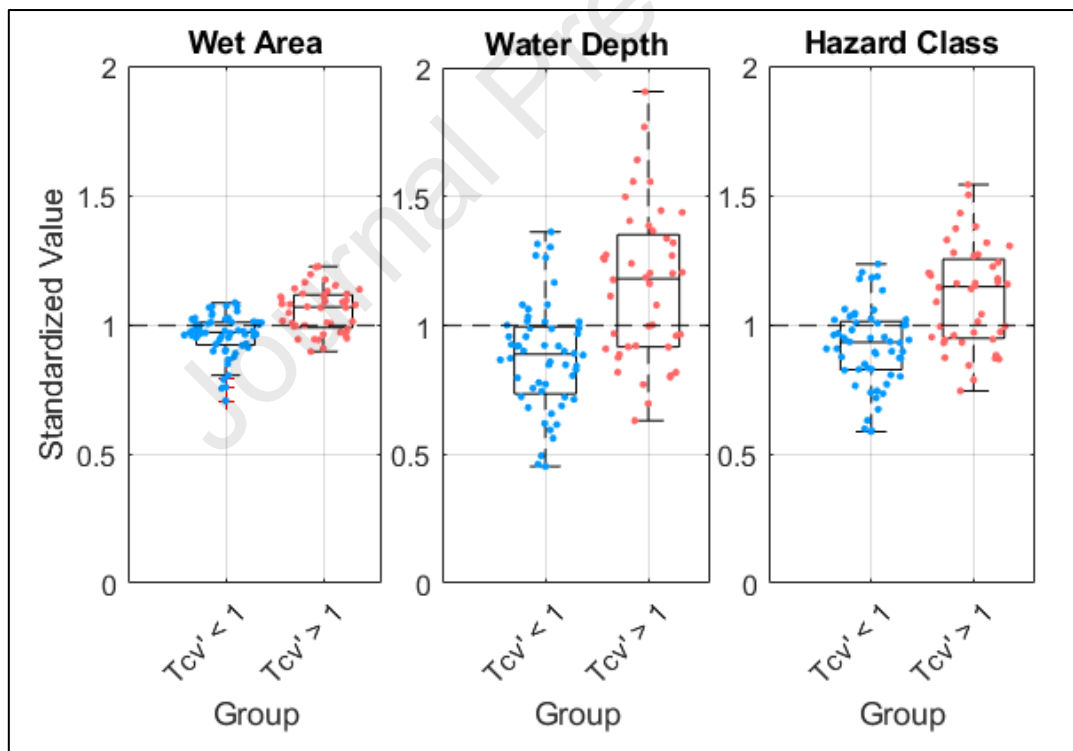


511

512 **Figure 12.** Hydrodynamic impacts in terms of standardized inundated area, spatial average of the maximum depths,  
 513 spatial average of AIDR hazard category. Significance test (T-test) applied to the  $S_H-T_H$  and  $S_L-T_H$  yields p-values  $< 0.05$   
 514 across all three impact variables confirming that the differences between the two clusters are statistically significant.

515 A comparison across the identified clusters yields three main insights.  
 516 Marked differences in variability are observed across the considered impact variables. Notably, among  
 517 hydrological metrics, peak discharge exhibits the highest variability, although this does not consistently  
 518 translate into proportional differences in hydrodynamic impacts. Moreover, there is a clear tendency for the  
 519  $S_H-T_H$  and  $S_L-T_H$  groups to be associated with above-average impacts, while the remaining two clusters  
 520 generally correspond to lower-impact scenarios. This distinction is statistically supported by the results of a

521 significance test (T-test) applied to the  $S_H-T_H$  and  $S_L-T_H$  groups, yielding p-values  $< 0.05$  across all three impact  
 522 variables. Furthermore, the  $S_H-T_H$  cluster is underrepresented, suggesting it may be either less frequent or less  
 523 relevant within the ensemble. Building on the previous findings, a simplified binary classification of the  
 524 scenarios is introduced, based on their standardized temporal variability ( $Tcv'$ ): Scenarios with  $Tcv' < 1$ ,  
 525 associated on average with less severe impacts; Scenarios with  $Tcv' > 1$ , associated on average with more  
 526 severe impacts. Focusing on hydrodynamic impacts, Figure 13 presents combined boxplots and swarmplots of  
 527 standardized impact metrics, grouped according to the two subsets:  $Tcv' < 1$  and  $Tcv' > 1$ . Within the two  
 528 subgroups, the distributions of the variables representing hydrodynamic impacts show minimally overlapping  
 529 interquartile ranges (IQRs) and clearly distinct median values. This distinction is further supported by the  
 530 results of a t-test, which yields p-values  $< 0.05$  for all the impact metrics, confirming that the observed  
 531 differences between the two groups are statistically significant.



532

533 **Figure 13.** Hydrodynamic impacts: standardized inundated area, spatial average of the maximum depths, spatial average  
 534 of AIDR hazard class. Significance test (T-test) applied to the  $Tcv' < 1$  subset and  $Tcv' > 1$  subset yields p-values  $< 0.05$   
 535 across all three impact variables confirming that the differences between the two clusters are statistically significant.

## 536 **4.4 Application of the Storm Variability Diagram for reducing uncertainty in impact-oriented** 537 **nowcasting**

### 538 *4.4.1 Ensemble based predicted hazard maps*

539 From an operational, impact based-forecasting perspective, these findings suggest the potential to simplify the  
540 representation of street-level flood hazard by defining only two representative maps, derived from the IQR of  
541 the two  $Tcv'$ -based clusters. The first map, based on the IQR of scenarios with  $Tcv' < 1$ , is representative of a  
542 medium-to-low impact scenarios, while the second, based on the IQR of scenarios with  $Tcv' > 1$ , corresponds  
543 to a medium-to-high impact scenario.

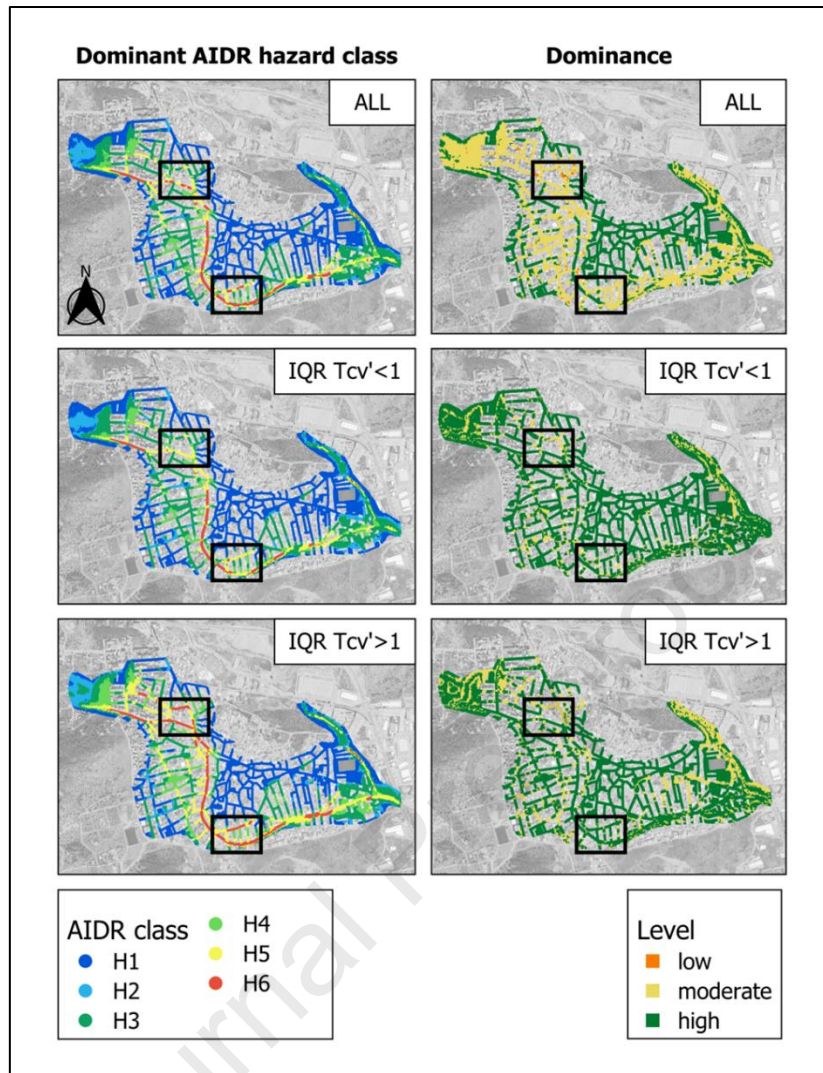
544 To evaluate how the uncertainty captured by the full ensemble compares with that of the two IQR-based  
545 reference maps informed by the Storm Variability Diagram, Figure 14 illustrates the spatial distribution of the  
546 dominant AIDR hazard class, i.e., the most frequently predicted class at each grid cell across the ensemble,  
547 and its corresponding degree of dominance, expressed as the percentage of ensemble members agreeing on  
548 that class. Dominance levels are categorized as Low (0–33%), Medium (33–67%), and High (67–100%). The  
549 comparison is shown for the full ensemble as well as for the two IQR-based scenario subsets ( $Tcv' < 1$  and  
550  $Tcv' > 1$ ).

551 A key finding is the significant increase in dominance when the ensemble is partitioned according to the Storm  
552 Variability Diagram. The map for the entire ensemble (top right) shows predominantly moderate agreement,  
553 indicating considerable uncertainty. Despite this difference in agreement, the resulting dominant hazard maps  
554 (left panels) are remarkably similar, consistently identifying the paths of highest hazard (H5-H6).

555 The analysis of agreement levels between the real-case AIDR classification and (i) the full ensemble, (ii) IQR  
556 subset IQR subset  $Tcv' > 1$  (higher impact storms), and (iii) and  $Tcv' < 1$  (lower-impact storms) reveals  
557 meaningful differences in spatial agreement (Table 2).

558 Notably, the IQR subsets exhibit a substantially higher proportion of high agreement between simulations  
559 compared to the full ensemble, which reflects the broader variability inherent in the entire stochastic set. This  
560 implies that ensemble-based nowcasting can benefit from clustering based on the Storm Variability diagram to  
561 reduce uncertainty and improve the reliability of impact predictions.

562



563

564 **Figure 14.** Maps of the dominant AIDR hazard class (left) and corresponding agreement levels (right) for the full  
 565 ensemble (top), the IQR subset with  $T_{cv}' < 1$  (center), and the IQR subset with  $T_{cv}' > 1$  (bottom). Black rectangles  
 566 highlight areas where both the dominant hazard level and its associated dominance vary depending on the scenario  
 567 subset, indicating transitions in predicted hazard class.

Agreement	Total ensemble	$T_{cv}' < 1$	$T_{cv}' > 1$
Low	0.5%	0.0%	0.0%
Moderate	52.0%	16.1%	26.4%
High	47.5%	83.9%	73.6%

568 **Table 2.** Percentage of the spatial domain falling within each level of agreement in terms of AIDR flood hazard  
 569 classification and: (i) the full stochastic ensemble, (ii) IQR subset  $T_{cv}' > 1$  (higher-impact scenarios), and  $T_{cv}' < 1$  (lower-  
 570 impact scenarios).

571 *4.4.2 Comparison between predicted hazard maps and real-based hazard patterns*

572 The impacts simulated using the historical rainfall event were not included in Figs. 11–13, as those analyses  
 573 were explicitly designed to investigate ensemble-based impact distributions. This ensemble analysis  
 574 represented a necessary preliminary step to first elucidate the interpretative potential of the Storm Variability  
 575 Diagram and, subsequently, to introduce the operational tool represented by the hazard maps shown in Figure  
 576 14, based on only one metric ( $Tcv'$ ), which constitute the core innovation of this work.

577 Once this ensemble-based framework was established, its operational consistency can be assessed by verifying  
 578 whether the expected impact scenarios inferred from rainfall structure is consistent with observed outcomes.  
 579 For this purpose, the historical event was introduced in this section not as a benchmark for model validation,  
 580 but as an independent reference to test the coherence of the proposed interpretation framework.

581 Specifically, Figure 14 represented the main operational output of the proposed methodology, showing that the  
 582 expected hazard pattern, characterised by reduced spatial variability, depends on the value of  $Tcv'$ . In this  
 583 context, the historical rainfall event was characterised by  $Tcv = 1.16$  and  $Tcv' = 0.935$ . Our framework therefore  
 584 statistically favoured the  $Tcv' < 1$  ensemble scenario as the most plausible structural pattern for its impacts.  
 585 Accordingly, the following analysis aimed to demonstrate that the hazard map derived from the observed event  
 586 exhibited a higher degree of similarity with the ensemble-based hazard scenario expected for  $Tcv' < 1$  than  
 587 with alternative scenarios ( $Tcv' > 1$ ).

588 The comparison is based on the Critical Success Index (CSI) and Hit Rate (HR), as defined in Eqs. 9 and 10,  
 589 respectively. These metrics evaluate the spatial overlap between the hazard map resulting from the simulation  
 590 based on historical rainfall and each reference map, based on the IQR subsets.

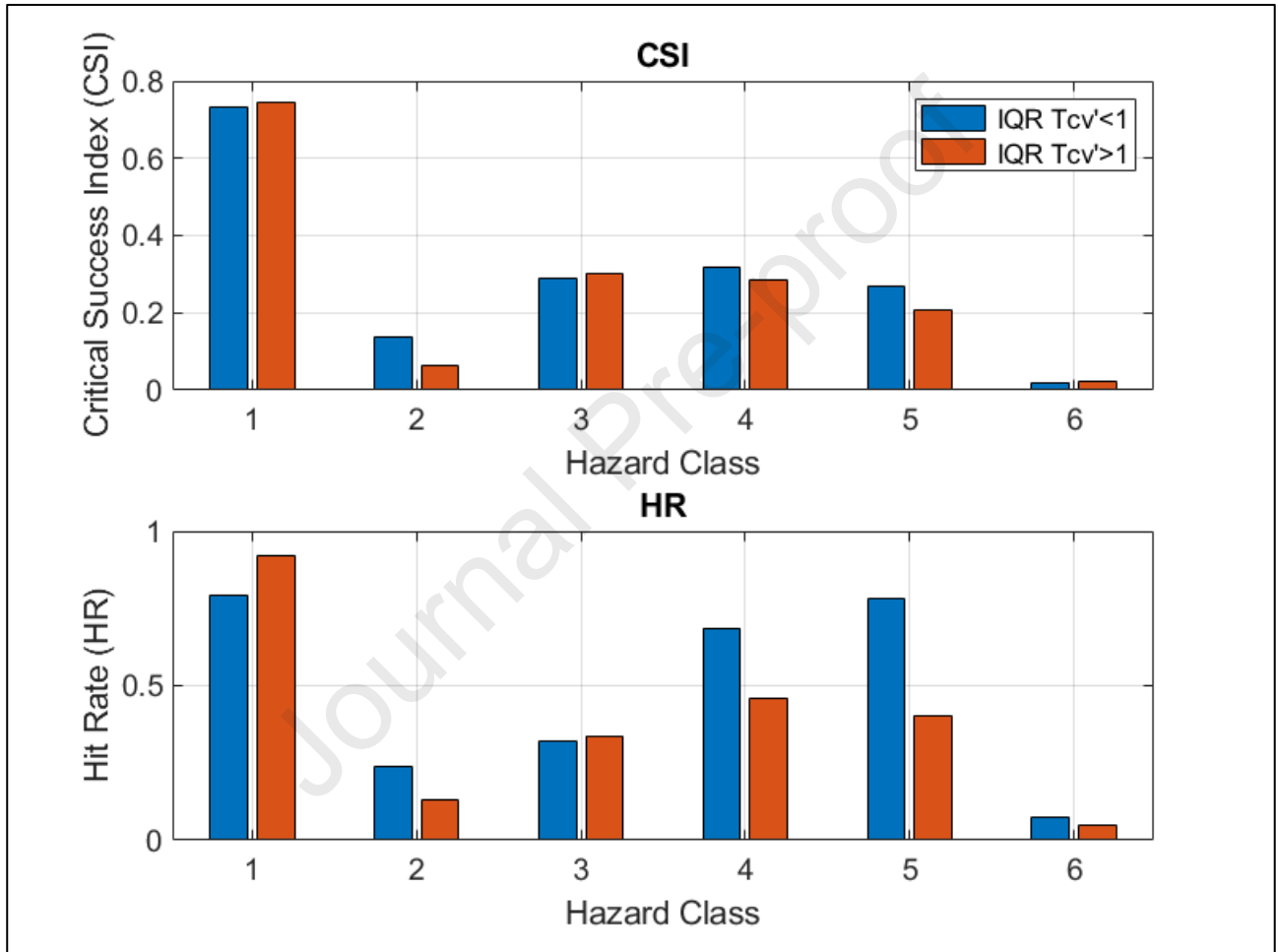
$$591 \quad CSI = \frac{Areal \cap Aref}{Areal \cup Aref} \quad (9)$$

$$592 \quad HR = \frac{Areal \cap Aref}{Aref} \quad (10)$$

593 Where *Areal* represents the area related to the simulation based on historical radar rainfall and *Aref* is the  
 594 ensemble-based reference.

595 Figure 15 presents the CSI and HR values for the AIDR hazard classes, derived from the comparison between  
 596 the output map from the simulation based on historical radar rainfall and the IQR mean maps corresponding

597 to  $T_{cv}' < 1$  and  $T_{cv}' > 1$ , respectively. The IQR mean map for  $T_{cv}' < 1$  consistently achieves higher CSI and  
 598 HR values across most hazard classes (H1 through H6). This is especially evident for H4, H5, and H6 (high  
 599 and very high hazard) in terms of both CSI and HR. These findings indicate a stronger alignment of the  
 600 observed scenario with the group of scenarios associated with expected low to medium impacts, consistently  
 601 with expectations based on the  $T_{cv}$  value of the observed event.  
 602



603  
 604 **Figure 15.** Hit Rate and Critical Success Index as measure of overlapping of the areas belonging to the different AIDR  
 605 hazard classes. The output of the simulation based on historical radar rainfall is compared to the mean IQR of the  $T_{cv}' < 1$   
 606 (low to medium impacts expected) and to the mean IQR of the  $T_{cv}' > 1$  (medium to high impacts expected)

## 607 5. Discussion

608 The results shown in this work offer a pathway to manage and reduce rainfall uncertainty in operational  
 609 nowcasting contexts. Herein we discuss the three research questions posed in the introduction, based on the

610 key results derived from this perspective, we highlight their implications, while we outline the limitations and  
611 future directions.

## 612 **5.1 Uncertainty at the watershed and street scales: Comparing Hydrological and** 613 **Hydrodynamic Variability**

614 Despite the stochastic generator's ability to reproduce the statistical properties and spatiotemporal correlations  
615 of the historical rainfall event, the resulting ground-level impacts exhibit remarkable variability. This finding  
616 has profound implications for flood forecasting: it demonstrates that statistical consistency at the  
617 meteorological level does not guarantee predictable outcomes at the impact level. Two rainfall events with  
618 identical statistical signatures can produce significantly different flooding scenarios. This disconnect between  
619 meteorological similarity and impact diversity highlights a critical gap in current forecasting approaches that  
620 rely heavily on return period estimates or statistical rainfall characteristics. The results suggest that the internal  
621 structure and organization of rainfall events plays a decisive role in determining flood severity.

622 A primary finding of this study is the significant difference in the magnitude of variability observed between  
623 the two scales of analysis: the watershed and the street scale. The analysis reveals that the hydrodynamic  
624 response is substantially less variable than the hydrological response. While the flood hydrographs show a  
625 considerable degree of uncertainty (with a  $CV$  up to 0.53), the final impact maps exhibit a much higher level  
626 of stability (average  $CV$  around 0.25). This suggests that while the catchment's hydrological response is highly  
627 sensitive to the rainfall's spatio-temporal structure, the subsequent propagation of runoff through the urban  
628 fabric exerts a dominant stabilizing effect. The interaction of the flow with micro-topography (buildings, roads)  
629 introduces diffusion and storage processes that lead to more consistent inundation patterns. This effect is  
630 further amplified by the hazard classification logic: the discretization of continuous depth and velocity values  
631 into a limited number of hazard classes acts as a final stabilizing step, making the impact map even more  
632 robust. The key implication of this finding is that direct impact indicators, such as street level hazard, are  
633 inherently less sensitive to rainfall organization and thus more suitable, for providing actionable, spatially  
634 consistent guidance for warning system and emergency management compared to aggregated hydrological  
635 metrics (like peak flow), which remain more sensitive to the initial rainfall variability.

636 Finally, it is important to note that the synthetic events generated by anySim exhibit limited variability in total  
637 rainfall volume across the ensemble (coefficient of variation  $< 10\%$ ), as a direct consequence of the stochastic  
638 generation process aimed at reproducing the statistical properties of the observed event. This constrained  
639 volume variability is intentional and reflects the framework's focus on exploring the impact of rainfall  
640 spatiotemporal structure rather than total volume differences. For this reason, correlations between total rainfall  
641 volume and hydrological/hydrodynamic response metrics are not pursued in this study. Such correlations  
642 would be potentially misleading for two reasons: (i) volume differences are not a dominant source of variability  
643 within the ensemble ( $CV < 10\%$ ), and (ii) several impact metrics (e.g., Vol\_A, Qp\_A) are evaluated at upstream  
644 cross-sections where spatial organization of rainfall relative to the drainage network plays a more critical role  
645 than basin-total volume. Future multi-event studies incorporating storms with wider volume ranges could  
646 disentangle the relative contributions of volume versus structure to flood variability.

## 647 **5.2 Linking Rainfall Structure and Hydrodynamic Impact**

648 To understand which rainfall characteristics are the most influential to the severity of impacts, a correlation  
649 analysis was conducted between a set of descriptive rainfall metrics and various impact indicators. Among all  
650 the metrics analysed, spatial variability ( $Scv$ ) and, even more clearly, temporal variability ( $Tcv$ ), showed the  
651 most consistent, albeit moderate, correlations with the entire spectrum of impact metrics considered, both  
652 hydrological and hydrodynamic.

653 Based on this observation, the "Storm Variability Diagram" was introduced as a tool to visually explore this  
654 relationship. In the diagram, the axes represent the two variables ( $Tcv$  and  $Scv$ ) standardized by their mean  
655 value calculated over the entire ensemble of 100 realizations. The purpose of this standardization is to make  
656 the values dimensionless and comparable, and it naturally divides the diagram into four quadrants, depending  
657 on whether the  $Tcv$  and  $Scv$  values for a given scenario are above or below the ensemble mean.

658 This quadrant-based division, while fundamentally statistical, also offers a potential framework for physical  
659 interpretation (Aala et al., 2025). For instance, scenarios clustering in the  $S_L-T_H$  quadrant defined by above-  
660 average temporal and below-average spatial variability might be analogous to meteorological events  
661 characterized by spatially focused bursts, such as isolated severe cells. Conversely, events in the opposite  
662 quadrant could correspond to patterns resembling more extensive and steady rainfall, akin to stratiform

663 systems. Framing the statistical results in this way provides a potential meteorological key to interpretation,  
664 linking abstract variability metrics to a propensity for causing severe impacts, thereby adding a physically  
665 intuitive layer to the underlying statistical evidence.

666 However, it is crucial to emphasize that the Storm Variability Diagram should not be interpreted as a  
667 deterministic classification tool. Its purpose is not to assert that a storm with specific spatial ( $Scv$ ) and temporal  
668 ( $Tcv$ ) variability characteristics will necessarily produce an impact of a predetermined magnitude. Instead, the  
669 diagram must be understood from a probabilistic perspective. The grouping based on the quadrants indicates  
670 the higher or lower likelihood of observing ensemble realizations (and thus, flood scenarios) associated with a  
671 particular risk condition. For instance, a storm falling into a specific quadrant does not guarantee a "high-risk"  
672 outcome; rather, it signals that scenarios of severe impact are significantly more likely to be found within that  
673 cluster compared to others.

### 674 **5.3 Potential for forecasting/nowcasting applications**

675 The most application-oriented result is the possibility of using the rainfall structure to contextualize forecast  
676 uncertainty.

677 Identifying  $Tcv$  and  $Scv$  as the most influential predictors of impact variability provides a practical pathway to  
678 link rainfall structure to expected impact categories. This enables forecasters to interpret rainfall ensemble  
679 outputs not only in terms of cumulative depth or return period, but through physically meaningful descriptors  
680 of temporal concentration and spatial coherence. These variables can be computed rapidly from forecast  
681 rainfall fields, facilitating early, pre-simulation screening of scenarios likely to produce more severe impacts.

682 In particular, the analysis of the impact distribution within the quadrants of the Storm Variability Diagram  
683 revealed that the separation along the temporal variability axis ( $Tcv$ ) was the clearest in discriminating between  
684 events of medium to higher or medium to lower impact. This led directly to the binary classification that proved  
685 effective in reducing prediction uncertainty. The binary classification of scenarios based on a  $Tcv$  threshold  
686 value allowed for the grouping of simulations into two scenario-types with considerably higher internal spatial  
687 consistency (up to 84% agreement), compared to that of the entire ensemble (48%), with a reduced variability.  
688 This approach offers a practical methodology. Instead of relying on an ensemble of 100 simulations, a  
689 forecaster could use the  $Tcv$  of a rainfall forecast to place it within one of the two classes and associate it with

690 a pre-calculated hazard map. The verification performed using the observed radar data showed that the real  
691 impact map corresponded to that of the group predicted by the characteristics of the observed rainfall. This  
692 result supports the validity of the framework as a "proof-of-concept," suggesting a path to obtain rapid  
693 estimates of potential impact that account for uncertainty, without the need to run the entire set of simulations  
694 in real-time.

695 In previous work (Costabile et al., 2023), we showed that an impact-based flood warning system for Mandra,  
696 based on short-term weather forecasts (up to 3 h) using radar data and detailed hydrodynamic simulations, is  
697 feasible, assuming a computational cost of approximately 0.5 h. With the upgrade of our methodological  
698 approach to incorporate stochastic rainfall fields, we estimate that an early warning system with a 2 h lead time  
699 can be developed, provided that all equiprobable rainfall scenarios are simulated in parallel.

#### 700 **5.4 Study Limitations and Future Perspectives**

701 A fundamental limitation of this study is its reliance on a single case study, the 2017 Mandra flash flood. We  
702 acknowledge that the specific quantitative results may be intrinsically linked to the hydro-geomorphological  
703 characteristics of the Mandra catchment and to the specific meteorological nature of the analysed storm.  
704 Therefore, the findings presented should be interpreted as a detailed characterization for this specific event,  
705 rather than universally applicable principles. Future research is essential to validate and generalize these  
706 insights. The next logical step would be to apply the same framework to a diverse set of catchments with  
707 different characteristics and to a variety of storm types to investigate how the relationships between rainfall  
708 variability and flood impact change across different contexts. It should also be noted that the storm variability  
709 diagram is inherently tied to the rainfall generator employed, and future studies should investigate the influence  
710 of generator characteristics on the resulting outcomes, as well as the effect of the ensemble size on the results,  
711 which herein was set to 100, due to the significant computational effort associated with using a larger sized  
712 ensemble.

713 Moreover, the analysis focused solely on the uncertainty arising from the internal structure of the rainfall,  
714 keeping other important sources of variability constant, such as the initial soil moisture conditions or the  
715 hydrodynamic model parameters. In particular, the Green-Ampt infiltration scheme was maintained constant  
716 across all scenarios to isolate the effects of rainfall variability from soil moisture uncertainty. While this

717 prevents exploration of rainfall-infiltration interactions, it enables clear attribution of response variability to  
718 storm structure. Future work could incorporate stochastic infiltration parameters, though this would require  
719 additional validation data and significantly complicate interpretation. The framework's modular structure  
720 facilitates these enhancements without fundamental redesign. Alternative stochastic generators, infiltration  
721 schemes, or impact metrics can be substituted while maintaining the core uncertainty quantification approach.

## 722 6. Conclusions

723 This study developed a Stochastic Rain-on-Grid framework that couples high-resolution stochastic rainfall  
724 generation with 2D hydrodynamic modeling for assessing uncertainty in flash flood impact estimation and  
725 forecasting. While individual components exist in literature, their integration for impact-oriented uncertainty  
726 quantification represents a methodological advancement that bridges catchment-scale hydrological uncertainty  
727 with urban hydrodynamic impact assessment. The potential of this framework has been demonstrated for the  
728 2017 Mandra event, which serves not merely as a test case, but as a typical example of a complex, high-impact  
729 flash flood in a piedmont urbanized area, whose features combine both mountain and urban flood processes.  
730 In relation to the three research questions posed in the introduction, the overall analysis reveals several key  
731 findings, each of which highlights practical potential for warning systems and emergency management

- 732 • Research question Q1: substantial variability emerges in hydrological response ( $CV$  values exceeding  
733 0.50 for peak discharge) which systematically attenuates through the hydrodynamic model, yielding  
734 more stable hazard classifications (average  $CV \approx 0.25$ ). This hierarchical attenuation, occurring  
735 through the transformation made in cascade at both watershed level and urban district level, suggests  
736 that impact-based indicators are inherently more robust for operational warning systems than  
737 traditional hydrological metrics. Importantly, these indicators should capture the full range of possible  
738 outcomes rather than relying solely on deterministic hydrographs or return periods. Overall, these  
739 findings emphasize that the spatio-temporal structure of rainfall is a critical factor for warning systems  
740 and cannot be reduced to cumulative rainfall depth alone, highlighting the practical value of adopting  
741 impact-based approaches in emergency management.
- 742 • Research question Q2: the analysis of various rainfall structure metrics revealed that spatial coefficient  
743 of variation ( $Scv$ ) and particularly temporal coefficient of variation ( $Tcv$ ) showed moderate but

744 consistent correlations with both hydrological and hydrodynamic impact indicators, providing  
745 physically-based proxies for expected flood severity under equiprobable rainfall scenarios. Building  
746 on the observed correlations between  $T_{cv}$  and  $S_{cv}$  with impact severity, we developed the Storm  
747 Variability Diagram, structured upon the no dimensional values of  $T_{cv}$  and  $S_{cv}$  using their mean values,  
748 that successfully statistically classifies equiprobable events by their expected impact magnitude.  
749 Specifically, when scenarios were grouped according to the diagram's quadrants, clear correlations  
750 emerged between storm variability patterns and impact severity, thus enabling a pre-simulation  
751 screening of scenarios likely to produce more severe impacts. While storm space-time structure  
752 represents the primary driver of these differences, it is plausible that the small variability in total  
753 rainfall volume within the ensemble may also exert a secondary influence on the results.

- 754 • Research question Q3: the interpretation of the Storm Variability Diagram as tool to provide  
755 probabilistic relations between rainfall organization and characteristic hydrological and hydrodynamic  
756 responses, potentially offer a practical pathway to reduce ensemble uncertainty in operational  
757 nowcasting systems. Specifically, further binary classification based on standardized  $T_{cv}$  values  
758 ( $T_{cv}' > 1$  vs  $T_{cv}' < 1$ ) enabled generation of distinct hazard maps with significantly greater spatial  
759 agreement (up to 84% high agreement vs 48% for the full ensemble) and reduced uncertainty. The  
760 framework's predictive capability was verified by demonstrating that the hazard map simulated using  
761 the observed radar data corresponds to one of the two binary classification groups, in coherence with  
762 the rainfall structure characteristics of the original radar observations. This consistency confirms the  
763 diagram's ability to link rainfall structure to impact patterns and supports its potential for rapid  
764 uncertainty assessment without computationally expensive full ensemble simulations.

765 In summary, this study establishes a *proof-of-concept* for an impact-oriented approach in managing rainfall  
766 uncertainty. A main limitation is that the framework was demonstrated on a single flash-flood event, so its  
767 quantitative findings may be specific to the hydro-geomorphological and meteorological characteristics of the  
768 Mandra basin. Extending the analysis to multiple catchments and storm typologies is therefore essential to  
769 assess generality. Similarly, integrating spatial variability of soil moisture, uncertainties in radar measurements,  
770 and hydrodynamic modelling parameters into a multi-source uncertainty framework represents a natural next  
771 step. Finally, assessing the operational use of the proposed classification scheme with rainfall forecasts will be

772 important to evaluate its real-time nowcasting performance. These directions collectively support the  
 773 development of robust, computationally efficient, impact-based flash-flood forecasting systems.

774

## 775 References

- 776 Aala, S., Kumar, R., Ribbe, L., Borchardt, D., & Tarasova, L. (2025). The Effects of Space–Time Dynamics of  
 777 Precipitation on the Shape and Timing of Streamflow Event Hydrographs. *Hydrological Processes*, 39(11), e70333.
- 778 AIDR (2017). Flood hazard. In Australian Disaster Resilience Handbook Collection. Guideline 7 – 3. Retrieved from  
 779 <https://knowledge.aidr.org.au/media/3521/adr-handbook-7.pdf>
- 780 Agonafir C., Zheng T., 2025. Structured exploration of machine learning model complexity for spatio-temporal  
 781 forecasting of urban flooding. *Urban Water Journal*. <https://doi.org/10.1080/1573062X.2025.2589078>
- 782 Ailliot, P., Allard, D., Monbet, V., & Naveau, P. (2015). Stochastic weather generators: an overview of weather type  
 783 models. *Journal de la société française de statistique*, 156(1), 101–113.
- 784 Amengual, A., Borga, M., Ravazzani, G., & Crema, S. (2021). The Role of Storm Movement in Controlling Flash Flood  
 785 Response: An Analysis of the 28 September 2012 Extreme Event in Murcia, Southeastern Spain. *Journal of*  
 786 *Hydrometeorology*, 22(9), 2379–2392. <https://doi.org/10.1175/JHM-D-21-0001.1>
- 787 Apel, H., Vorogushyn, S., & Merz, B. (2022). Brief communication: Impact forecasting could substantially improve the  
 788 emergency management of deadly floods: case study July 2021 floods in Germany. *Natural Hazards and Earth*  
 789 *System Sciences*, 22(9), 3005–3014. <https://doi.org/10.5194/nhess-22-3005-2022>
- 790 Bárdossy A, Pegram G (2009) Copula based multisite model for daily precipitation simulation. *Hydrol Earth Syst Sci*  
 791 *Discuss* 6:4485–4534. <https://doi.org/10.5194/hessd-6-4485-2009>
- 792 Bellos, V., & Tsakiris, G. (2016). A hybrid method for flood simulation in small catchments combining hydrodynamic  
 793 and hydrological techniques. *Journal of Hydrology*, 540, 331–339. <https://doi.org/10.1016/j.jhydrol.2016.06.040>
- 794 Bellos, V., Costanzo, C., Kalogiros, J., Ahmadian, R., Rozos, E., & Costabile, P. (2025). Nowcasting Floods in Detailed  
 795 Scales Considering the Uncertainties Associated with impact-based Practical Applications. *Water Resources*  
 796 *Management*, 39(8), 4205–4225. <https://doi.org/10.1007/s11269-024-03988-5>
- 797 Bellos, V., Papageorgaki, I., Kourtis, I., Vangelis, H., Kalogiros, I., & Tsakiris, G. (2020). Reconstruction of a flash flood  
 798 event using a 2D hydrodynamic model under spatial and temporal variability of storm. *Natural Hazards*, 101(3),  
 799 711–726. <https://doi.org/10.1007/s11069-020-03891-3>
- 800 Benoit, L., Allard, D., & Mariethoz, G. (2018). Stochastic Rainfall Modeling at Sub-kilometer Scale. *Water Resources*  
 801 *Research*, 54(6), 4108–4130. <https://doi.org/10.1029/2018WR022817>
- 802 Berne, A., Delrieu, G., Creutin, J. D., & Obled, C. (2004). Temporal and spatial resolution of rainfall measurements  
 803 required for urban hydrology. *Journal of Hydrology*, 299(3–4), 166–179.  
 804 <https://doi.org/10.1016/j.jhydrol.2004.08.002>
- 805 Beven KJ, 2012. Rainfall-runoff modeling: The primer. John Wiley and Sons, New York, pp 360
- 806 Borga, M., Stoffel, M., Marchi, L., Marra, F., & Jakob, M. (2014). Hydrogeomorphic response to extreme rainfall in  
 807 headwater systems: Flash floods and debris flows. *Journal of Hydrology*, 518(PB), 194–205.  
 808 <https://doi.org/10.1016/j.jhydrol.2014.05.022>
- 809 Bournas A., Baltas E. (2025). Flood Hazard Assessment Using Weather Radar Data in Athens, Greece. *Remote Sensing*,  
 810 17 (1), art. no. 72. DOI: 10.3390/rs17010072
- 811 Bras RL, Rodríguez-Iturbe I (1985) Random functions and hydrology. Addison-Wesley, Reading, Mass
- 812 Breinl, K., Turkington T., Stowasser, M. (2013). Stochastic generation of multi-site daily precipitation for applications in  
 813 risk management. *Journal of Hydrology*, 498 (23–35). <https://doi.org/10.1016/j.jhydrol.2013.06.015>

- 814 Bruni, G., Reinoso, R., Van De Giesen, N. C., Clemens, F. H. L. R., & Ten Veldhuis, J. A. E. (2015). On the sensitivity of  
815 urban hydrodynamic modelling to rainfall spatial and temporal resolution. *Hydrology and Earth System Sciences*, 19(2),  
816 691-709.
- 817 Burton, A., Fowler, H. J., Blenkinsop, S., & Kilsby, C. G. (2010). Downscaling transient climate change using a Neyman–  
818 Scott Rectangular Pulses stochastic rainfall model. *Journal of Hydrology*, 381(1-2), 18-32.  
819 <https://doi.org/10.1016/j.jhydrol.2009.10.031>
- 820 Buttinger-Kreuzhuber, A., Konev, A., Horváth, Z., Cornel, D., Schwerdorf, I., Blöschl, G., & Waser, J. (2022). An  
821 integrated GPU-accelerated modeling framework for high-resolution simulations of rural and urban flash floods.  
822 *Environmental Modelling & Software*, 156, 105480. <https://doi.org/10.1016/j.envsoft.2022.105480>
- 823 Cao X., Qi Y., Ni G. (2023). X-band polarimetric radar QPE for urban hydrology: The increased contribution of high-  
824 resolution rainfall capturing. *Journal of Hydrology*, 617, art. no. 128905, DOI: 10.1016/j.jhydrol.2022.128905
- 825 Caviedes-Voullième, D., Morales-Hernández, M., Norman, M. R., & Özgen-Xian, I. (2023). SERGHEI (SERGHEI-  
826 SWE) v1. 0: a performance-portable high-performance parallel-computing shallow-water solver for hydrology and  
827 environmental hydraulics. *Geoscientific model development*, 16(3), 977-1008. [https://doi.org/10.5194/gmd-16-977-  
828 2023](https://doi.org/10.5194/gmd-16-977-2023)
- 829 Cea, L., & Bladé, E. (2015). A simple and efficient unstructured finite volume scheme for solving the shallow water  
830 equations in overland flow applications. *Water Resources Research*, 51(7), 5464–5486.  
831 <https://doi.org/10.1002/2014WR016547>
- 832 Cea, L., Álvarez, M., & Puertas, J. (2024). Using integrated hydrological-hydraulic modelling and global data sources to  
833 analyse the February 2023 floods in the Umbeluzi catchment (Mozambique). *Natural Hazards and Earth System  
834 Sciences*, 24(1), 225–243. <https://doi.org/10.5194/nhess-24-225-2024>
- 835 Chen, G., Hou, J., Hu, Y. et al. (2023). Simulated Investigation on the Impact of Spatial–temporal Variability of  
836 Rainstorms on Flash Flood Discharge Process in Small Watershed. *Water Resources Management* 37, 995–1011.  
837 <https://doi.org/10.1007/s11269-022-03398-5>
- 838 Chen, G., Hou, J., Wang, T., Lv, J., Jing, J., Ma, X., Yang, S., Deng, C., Ma, Y., & Ji, G. (2022). The effect of spatial-  
839 temporal characteristics of rainfall on urban inundation processes. *Hydrological Processes*, 36(8).  
840 <https://doi.org/10.1002/hyp.14655>
- 841 Costabile, P., Costanzo, C., & Macchione, F. (2013). A storm event watershed model for surface runoff based on 2D fully  
842 dynamic wave equations. *Hydrological Processes*, 27(4), 554–569. <https://doi.org/10.1002/hyp.9237>
- 843 Costabile P., Costanzo C., Ferraro D., Barca P. (2021). Is HEC-RAS 2D accurate enough for storm-event hazard  
844 assessment? Lessons learnt from a benchmarking study based on rain-on-grid modelling. *Journal of Hydrology*,  
845 603, art. no. 126962. DOI: 10.1016/j.jhydrol.2021.126962
- 846 Costabile, P., Costanzo, C., Kalogiros, J., & Bellos, V. (2023). Toward Street-Level Nowcasting of Flash Floods Impacts  
847 Based on HPC Hydrodynamic Modeling at the Watershed Scale and High-Resolution Weather Radar Data. *Water  
848 Resources Research*, 59(10). <https://doi.org/10.1029/2023WR034599>
- 849 Costabile, P., Costanzo, C., Lombardo, M., Shavers, E., & Stanislawski, L. V. (2024). Unravelling spatial heterogeneity  
850 of inundation pattern domains for 2D analysis of fluvial landscapes and drainage networks. *Journal of Hydrology*,  
851 632(June 2023), 130728. <https://doi.org/10.1016/j.jhydrol.2024.130728>
- 852 Costabile, P., Lombardo, M., Chiaravalloti, F., Caloiero, T., & Costanzo, C. (2026). Predicting pluvial flood impacts in  
853 data-scarce urban environments: Uncertainty and interplay between rainfall inputs and conceptual drainage loss  
854 models. *Urban Climate*, 65, 102724. <https://doi.org/10.1016/j.uclim.2025.102724>
- 855 Cristiano, E., ten Veldhuis, M. C., & Van De Giesen, N. (2017). Spatial and temporal variability of rainfall and their  
856 effects on hydrological response in urban areas—a review. *Hydrology and Earth System Sciences*, 21(7), 3859-3878.  
857 DOI: 10.5194/hess-21-3859-2017
- 858 Cristiano, E., ten Veldhuis, M. Claire, Wright, D. B., Smith, J. A., & van de Giesen, N. (2019). The Influence of Rainfall  
859 and Catchment Critical Scales on Urban Hydrological Response Sensitivity. *Water Resources Research*, 55(4),  
860 3375–3390. <https://doi.org/10.1029/2018WR024143>
- 861 de Moraes, O. L. L. (2023). An impact-based forecast system developed for hydrometeorological hazards. *International  
862 Journal of Disaster Risk Reduction*, 93(June), 103803. <https://doi.org/10.1016/j.ijdrr.2023.103803>
- 863 Diakakis, M., Andreadakis, E., Nikolopoulos, E. I., Spyrou, N. I., Gogou, M. E., Deligiannakis, G., Katsetsiadou, N. K.,  
864 Antoniadis, Z., Melaki, M., Georgakopoulos, A., Tsaprouni, K., Kalogiros, J., & Lekkas, E. (2019). An integrated

- 865 approach of ground and aerial observations in flash flood disaster investigations. The case of the 2017 Mandra flash  
 866 flood in Greece. *International Journal of Disaster Risk Reduction*, 33(October 2018), 290–309.  
 867 <https://doi.org/10.1016/j.ijdrr.2018.10.015>
- 868 Emmanuel, I., Andrieu, H., Leblois, E., & Flahaut, B. (2012). Temporal and spatial variability of rainfall at the urban  
 869 hydrological scale. *Journal of Hydrology*, 430–431, 162–172. <https://doi.org/10.1016/j.jhydrol.2012.02.013>
- 870 Emmanuel, I., Andrieu, H., Leblois, E., Janey, N., & Payrastre, O. (2015). Influence of rainfall spatial variability on  
 871 rainfall-runoff modelling: Benefit of a simulation approach? *Journal of Hydrology*, 531, 337–348.  
 872 <https://doi.org/10.1016/j.jhydrol.2015.04.058>
- 873 Ennouini, W., Fenocchi, A., Petaccia, G., Persi, E., & Sibilla, S. (2024). A complete methodology to assess hydraulic risk  
 874 in small ungauged catchments based on HEC-RAS 2D Rain-On-Grid simulations. *Natural Hazards*, 120(8), 7381–  
 875 7409. <https://doi.org/10.1007/s11069-024-06515-2>
- 876 Fernández-Pato, J., Caviedes-Voullième, D., & García-Navarro, P. (2016). Rainfall/runoff simulation with 2D full shallow  
 877 water equations: Sensitivity analysis and calibration of infiltration parameters. *Journal of Hydrology*, 536, 496–  
 878 513. <https://doi.org/10.1016/j.jhydrol.2016.03.021>
- 879 Godara, N., Bruland, O., & Alfredsen, K. (2024). Comparison of two hydrodynamic models for their rain-on-grid  
 880 technique to simulate flash floods in steep catchment. *Frontiers in Water*, 6(May), 1–17.  
 881 <https://doi.org/10.3389/frwa.2024.1384205>
- 882 Gyasi-Agyei, Y. (2005) Stochastic disaggregation of daily rainfall into one-hour time scale. *Journal of Hydrology*  
 883 309:178–190. <https://doi.org/10.1016/j.jhydrol.2004.11.018>
- 884 Hosking JRM (1990) L-Moments: Analysis and Estimation of Distributions Using Linear Combinations of Order  
 885 Statistics. *J R Stat Soc Ser B* 52:105–124
- 886 Kaltenberger, R., Schaffhauser, A., & Staudinger, M. (2020). What the weather will do—results of a survey on impact-  
 887 oriented and impact-based warnings in European NMHSs. *Advances in Science and Research*, 17, 29–38.  
 888 <https://doi.org/10.5194/asr-17-29-2020>
- 889 Kalogiros, J., Anagnostou, M. N., Anagnostou, E. N., Montopoli, M., Picciotti, E., & Marzano, F. S. (2013). Correction  
 890 of polarimetric radar reflectivity measurements and rainfall estimates for apparent vertical profile in stratiform  
 891 rain. *Journal of applied meteorology and climatology*, 52(5), 1170–1186. <https://doi.org/10.1175/JAMC-D-12-0140.1>
- 893 Khosh Bin Ghomash, S, Bachmann, D., Caviedes-Voullième, D., & Hinz, C. (2022). Impact of Rainfall Movement on  
 894 Flash Flood Response: A Synthetic Study of a Semi-Arid Mountainous Catchment. *Water (Switzerland)*, 14(12), 1–  
 895 25. <https://doi.org/10.3390/w14121844>
- 896 Khosh Bin Ghomash, S., Apel, H., Schröter, K., & Steinhausen, M. (2025). Rapid high-resolution impact-based flood  
 897 early warning is possible with RIM2D: a showcase for the 2023 pluvial flood in Braunschweig. *Natural Hazards and*  
 898 *Earth System Sciences*, 25(5), 1737–1749. <https://doi.org/10.5194/nhess-25-1737-2025>
- 899 Kilsby, C. G., Jones, P. D., Burton, A., et al (2007). A daily weather generator for use in climate change studies. *Environ*  
 900 *Model Softw* 22:1705–1719. <https://doi.org/10.1016/j.envsoft.2007.02.005>
- 901 Kirstetter, G., Delestre, O., Lagree, P.-Y., Popinet, S., & Josserand, C. (2021). B-flood 1.0: An open-source Saint-Venant  
 902 model for flash-flood simulation using adaptive refinement. *Geoscientific Model Development*, 14(11), 7117–7132.  
 903 <https://doi.org/10.5194/gmd-14-7117-2021>
- 904 Kossieris P, Makropoulos C, Onof C, Koutsoyiannis D (2016). A rainfall disaggregation scheme for sub-hourly time  
 905 scales: Coupling a Bartlett-Lewis based model with adjusting procedures. *J Hydrol.*  
 906 <https://doi.org/10.1016/j.jhydrol.2016.07.015>
- 907 Koutsoyiannis, D. (1999). Optimal decomposition of covariance matrices for multivariate stochastic models in hydrology.  
 908 *Water Resources Research* 35:1219–1229. <https://doi.org/10.1029/1998WR900093>
- 909 Koutsoyiannis, D. (2000). A generalized mathematical framework for stochastic simulation and forecast of hydrologic  
 910 time series. *Water Resour Res* 36:1519–1533. <https://doi.org/10.1029/2000WR900044>
- 911 Koutsoyiannis, D. (2016). Generic and parsimonious stochastic modelling for hydrology and beyond. *Hydrol Sci J*  
 912 61:225–244. <https://doi.org/10.1080/02626667.2015.1016950>

- 913 Koutsoyiannis, D., Montanari, A. (2015). Negligent killing of scientific concepts: the stationarity case. *Hydrol Sci J*  
914 60:1174–1183. <https://doi.org/10.1080/02626667.2014.959959>
- 915 Lee, T., Salas, J.D. (2011). Copula-based stochastic simulation of hydrological data applied to Nile River flows. *Hydrol*  
916 *Res* 42:318–330. <https://doi.org/10.2166/nh.2011.085>
- 917 Lin, R., Zheng, F., Ma, Y., Duan, H. F., Chu, S., & Deng, Z. (2022). Impact of Spatial Variation and Uncertainty of Rainfall  
918 Intensity on Urban Flooding Assessment. *Water Resources Management*, 36(14), 5655–5673.  
919 <https://doi.org/10.1007/s11269-022-03325-8>
- 920 Llasat, M. C., Marcos, R., Llasat-Botija, M., Gilabert, J., Turco, M., & Quintana-Seguí, P. (2014). Flash flood evolution  
921 in North-Western Mediterranean. *Atmospheric Research*, 149, 230–243.  
922 <https://doi.org/10.1016/j.atmosres.2014.05.024>
- 923 Macchione, F., & Lombardo, M. (2021). Roughness-Based Method for Simulating Hydraulic Consequences of Both  
924 Woody Debris Clogging and Breakage at Bridges in Basin-Scale Flood Modeling. *Water Resources Research*,  
925 57(12). <https://doi.org/10.1029/2021WR030485>
- 926 Marchi, L., Borga, M., Preciso, E., & Gaume, E. (2010). Characterisation of selected extreme flash floods in Europe and  
927 implications for flood risk management. *Journal of Hydrology*, 394(1–2), 118–133.  
928 <https://doi.org/10.1016/j.jhydrol.2010.07.017>
- 929 Mehrotra R, Srikanthan R, Sharma A (2006) A comparison of three stochastic multi-site precipitation occurrence  
930 generators. *J Hydrol* 331:280–292. <https://doi.org/10.1016/j.jhydrol.2006.05.016>
- 931 Meng, D., Liao, Y., Deng, Z., Chen, Y., Lai, C., Chen, X., & Wang, Z. (2025). Spatially moving non-uniform rainstorms  
932 may exacerbate urban flooding disasters. *Journal of Hydrology*, 660(PA), 133374.  
933 <https://doi.org/10.1016/j.jhydrol.2025.133374>
- 934 Ming, X., Liang, Q., Xia, X., Li, D., & Fowler, H. J. (2020). Real-Time Flood Forecasting Based on a High-Performance  
935 2-D Hydrodynamic Model and Numerical Weather Predictions. *Water Resources Research*, 56(7).  
936 <https://doi.org/10.1029/2019WR025583>
- 937 Mitsopoulos, G., Diakakis, M., Panagiotatou, E., Sant, V., Bloutsos, A., Lekkas, E., Baltas, E., & Stamou, A. I.  
938 (2022). How would an extreme flood have behaved if flood protection works were built? The case of the  
939 disastrous flash flood of November 2017 in Mandra, Attica, Greece. *Urban Water Journal*, 19(11), 911–  
940 921. <https://doi.org/10.1080/1573062X.2022.2103002>
- 941 Montanari A, Koutsoyiannis D (2014) Modeling and mitigating natural hazards: Stationarity is immortal! *Water Resour*  
942 *Res* 50:9748–9756. <https://doi.org/10.1002/2014WR016092>
- 943 Mosimann, M., Kauzlaric, M., Schick, S., Martius, O., & Zischg, A. P. (2024). Evaluation of surrogate flood models for  
944 the use in impact-based flood warning systems at national scale. *Environmental Modelling and Software*,  
945 173(December 2023), 105936. <https://doi.org/10.1016/j.envsoft.2023.105936>
- 946 Mudholkar, G. S., & Srivastava, D. K. (1993). Exponentiated Weibull family for analyzing bathtub failure-rate data. *IEEE*  
947 *transactions on reliability*, 42(2), 299-302. doi: 10.1109/24.229504
- 948 Nelsen, R. B. (2006). *An introduction to copulas*. New York, NY: Springer New York.
- 949 Nikolopoulos, E. I., Borga, M., Zocatelli, D., & Anagnostou, E. N. (2014). Catchment-scale storm velocity:  
950 quantification, scale dependence and effect on flood response. *Hydrological Sciences Journal*, 59(7), 1363–1376.  
951 <https://doi.org/10.1080/02626667.2014.923889>
- 952 Ntiggakis, C., Markopoulos-Sarikas, G., Dimitriadis, P., Iliopoulou, T., Efstratiadis, A., Koukouvinos, A., Koussis, A.,  
953 Mazi, K., Katsanos, D., & Koutsoyiannis, D. (2018). Hydrological investigation of the catastrophic flood event in  
954 Mandra, Western Attica. *Geophysical Research Abstracts*, 20, EGU2018-17591-1. European Geosciences Union  
955 General Assembly 2018
- 956 Ochoa-Rodriguez S, Wang LP, Gires A, Pina RD, Reinoso-Rondinel R, Bruni G, Ichiba A, Gaitan S, Cristiano E, van  
957 Assel J, Kroll S, Murlà-Tuyls D, Tisserand B, Schertzer D, Tchiguirinskaia I, Onof C, Willems P, ten Veldhuis MC  
958 (2015). Impact of spatial and temporal resolution of rainfall inputs on urban hydrodynamic modelling outputs: A  
959 multi-catchment investigation. *Journal of Hydrology* 531:389–407. DOI: 10.1016/j.jhydrol.2015.05.035
- 960 Onof C, Chandler RE, Kakou A, et al (2000) Rainfall modelling using Poisson-cluster processes: a review of  
961 developments. *Stoch Environ Res Risk Assess* 14:0384–0411. <https://doi.org/10.1007/s004770000043>

- 962 Pan, X., Hou, J., Wang, T., Li, X., Jing, J., Chen, G., Qiao, J., & Guo, Q. (2024). Study on the Influence of Temporal and  
 963 Spatial Resolution of Rainfall Data on Watershed Flood Simulation Performance. *Water Resources Management*,  
 964 38(8), 2647–2668. <https://doi.org/10.1007/s11269-023-03661-3>
- 965 Paschalis, A., Fatichi, S., Molnar, P., Rimkus, S., & Burlando, P. (2014). On the effects of small scale space-time  
 966 variability of rainfall on basin flood response. *Journal of Hydrology*, 514, 313–327.  
 967 <https://doi.org/10.1016/j.jhydrol.2014.04.014>
- 968 Peleg, N., Ban, N., Gibson, M. J., Chen, A. S., Paschalis, A., Burlando, P., & Leitão, J. P. (2022). Mapping storm spatial  
 969 profiles for flood impact assessments. *Advances in Water Resources*, 166(May), 104258.  
 970 <https://doi.org/10.1016/j.advwatres.2022.104258>
- 971 Peleg, N., Blumensaat, F., Molnar, P., Fatichi, S., & Burlando, P. (2017). Partitioning the impacts of spatial and  
 972 climatological rainfall variability in urban drainage modeling. *Hydrology and Earth System Sciences*, 21(3), 1559–  
 973 1572. <https://doi.org/10.5194/hess-21-1559-2017>
- 974 Pentakota L., Wadhwa A., Das Bhowmik R., Mujumdar P.P., (2025). A coupled high-resolution forecasting model for  
 975 urban floods. *Urban Water Journal*. <https://doi.org/10.1080/1573062X.2025.2560544>
- 976 Perez, G., Gomez-Velez, J. D., Chen, X., & Scheibe, T. (2023). The directional unit hydrograph model: Connecting  
 977 streamflow response to storm dynamics. *Journal of Hydrology*, 627(PA), 130422.  
 978 <https://doi.org/10.1016/j.jhydrol.2023.130422>
- 979 Perez, G., Gomez-Velez, J. D., Mantilla, R., Wright, D. B., & Li, Z. (2021). The Effect of Storm Direction on Flood  
 980 Frequency Analysis. *Geophysical Research Letters*, 48(9), 1–10. <https://doi.org/10.1029/2020GL091918>
- 981 Rajagopalan, B., Lall, U. (1999) A k-nearest-neighbor simulator for daily precipitation and other weather variables. *Water*  
 982 *Resour Res* 35:3089–3101. <https://doi.org/10.1029/1999WR900028>
- 983 Saharia, M., Kirstetter, P. E., Vergara, H., Gourley, J. J., Emmanuel, I., & Andrieu, H. (2021). On the Impact of Rainfall  
 984 Spatial Variability, Geomorphology, and Climatology on Flash Floods. *Water Resources Research*, 57(9), 1–18.  
 985 <https://doi.org/10.1029/2020WR029124>
- 986 Serinaldi, F. (2009). Copula-based mixed models for bivariate rainfall data: an empirical study in regression perspective.  
 987 *Stoch Environ Res Risk Assess* 23:677–693. <https://doi.org/10.1007/s00477-008-0249-z>
- 988 Song W., Guan M., Guo K., Yu D., (2025). Rapid flood inundation mapping by integrating deep learning-based image  
 989 super-resolution with coarse-grid hydrodynamic modelling. *Engineering Applications of Computational Fluid*  
 990 *Mechanics*, 19 (1), art. no. 2481115. <https://doi.org/10.1080/19942060.2025.2481115>
- 991 Stamou, A. I. (2018). The disastrous flash flood of Mandra in Attica-Greece and now what? *Civil Engineering Research*  
 992 *Journal*, 6(1), Article 555677. <https://doi.org/10.19080/CERJ.2018.06.555677>
- 993 Tarasova, L., Basso, S., Wendi, D., Viglione, A., Kumar, R., & Merz, R. (2020). A process-based framework to characterize  
 994 and classify runoff events: The event typology of Germany. *Water Resources Research*, 56,  
 995 e2019WR026951. <https://doi.org/10.1029/2019WR026951>
- 996 Tarpanelli, A., Franchini, M., Brocca, L., et al (2012) A simple approach for stochastic generation of spatial rainfall  
 997 patterns. *J Hydrol* 472–473:63–76. <https://doi.org/10.1016/j.jhydrol.2012.09.010>
- 998 Tsoukalas, I., Efstratiadis, A., Makropoulos, C. (2018a). Stochastic Periodic Autoregressive to Anything (SPARTA):  
 999 Modeling and simulation of cyclostationary processes with arbitrary marginal distributions. *Water Resour Res*  
 1000 54:161–185. <https://doi.org/10.1002/2017WR021394>
- 1001 Tsoukalas, I., Efstratiadis, A., Makropoulos, C. (2019). Building a puzzle to solve a riddle: A multi-scale disaggregation  
 1002 approach for multivariate stochastic processes with any marginal distribution and correlation structure. *J Hydrol*  
 1003 575:354–380. <https://doi.org/10.1016/j.jhydrol.2019.05.017>
- 1004 Tsoukalas, I., Kossieris, P., Makropoulos, C. (2020). Simulation of Non-Gaussian Correlated Random Variables,  
 1005 Stochastic Processes and Random Fields: Introducing the anySim R-Package for Environmental Applications and  
 1006 Beyond. *Water* 12:1645. <https://doi.org/10.3390/w12061645>
- 1007 Tsoukalas, I., Makropoulos, C., Koutsoyiannis, D. (2018b). Simulation of stochastic processes exhibiting any-range  
 1008 dependence and arbitrary marginal distributions. *Water Resour Res*. <https://doi.org/10.1029/2017WR022462>

- 1009 Varra, G., İnan, Ç. A., Della Morte, R., Tartaglia, M., Fiduccia, A., Zammuto, A., Agostino, I., & Cozzolino, L. (2025).  
 1010 Assessment of direct rainfall and flood-induced damage to land transport infrastructure using two-dimensional  
 1011 HEC-RAS 6.6 rain-on-grid simulations. *Natural Hazards*, 17615–17645. [https://doi.org/10.1007/s11069-025-](https://doi.org/10.1007/s11069-025-07484-w)  
 1012 [07484-w](https://doi.org/10.1007/s11069-025-07484-w)
- 1013 von Ruetze, J., P. Lehmann, and D. Or (2014), Effects of rainfall spatial variability and intermittency on shallow landslide  
 1014 triggering patterns at a catchment scale, *Water Resources Research* 50, 7780–7799, doi:10.1002/2013WR015122.
- 1015 Wang, F., Ouyang, C., An, H., Chen, X., Zhou, S., & Xu, Q. (2025). A flash flood numerical modeling and forecasting  
 1016 tool in mountainous small catchments based on a 2-D hydrodynamic model. *Earth and Space Science*, 12(7),  
 1017 e2024EA004076. <https://doi.org/10.1029/2024EA004076>
- 1018 Wang X., Xiao M., Liu Y., Guo J., Qin Y., Zhang Y., (2024). A rapid and efficient method for flash flood simulation based  
 1019 on deep learning. *Engineering Applications of Computational Fluid Mechanics*, 18 (1), art. no. 2407016.  
 1020 <https://doi.org/10.1080/19942060.2024.2407016>
- 1021 Wilks DS, Wilby RL (1999) The weather generation game: a review of stochastic weather models. *Prog Phys Geogr*  
 1022 23:329–357. <https://doi.org/10.1191/030913399666525256>
- 1023 WMO – World Meteorological Organization (2021). WMO Guidelines on Multi-hazard Impact-based Forecast and  
 1024 Warning Services. Technical Report: WMO-No. 1150. Available at: <https://library.wmo.int/idurl/4/57739>
- 1025 Wright, D. B., Yu, G., & England, J. F. (2020). Six decades of rainfall and flood frequency analysis using stochastic storm  
 1026 transposition: Review, progress, and prospects. *Journal of Hydrology*, 585(November 2019), 124816.  
 1027 <https://doi.org/10.1016/j.jhydrol.2020.124816>
- 1028 Wu X., Zhao Y., Zhang W., Li X., Qin G., Li H., 2025. Probabilistic early warning of flash floods using Monte Carlo  
 1029 simulation and hydrological modelling. *Engineering Applications of Computational Fluid Mechanics*, 19 (1), art.  
 1030 no. 2523423. <https://doi.org/10.1080/19942060.2025.2523423>.
- 1031 Xia, X., Liang, Q., & Ming, X. (2019). A full-scale fluvial flood modelling framework based on a high-performance  
 1032 integrated hydrodynamic modelling system (HiPIMS). *Advances in Water Resources*, 132, 103392.  
 1033 <https://doi.org/10.1016/j.advwatres.2019.103392>
- 1034 Xu, D., Bisht, G., Engwirda, D., Feng, D., Tan, Z., & Ivanov, V. Y. (2025a). Uncertainties in Simulating Flooding During  
 1035 Hurricane Harvey Using 2D Shallow Water Equations. *Water Resources Research*, 61(1).  
 1036 <https://doi.org/10.1029/2024WR038032>
- 1037 Xu, S., Wang, Q., Yu, J., Zhao, G., Ji, H., Yue, Q., Zheng, Y., Xu, H., Li, H., & Yao, X. (2025b). The impact of the  
 1038 spatiotemporal structure of rainfall on flood response over a piedmont urban basin: An approach coupling machine  
 1039 learning and hydrologic modeling. *Journal of Hydrology*, 659(August 2024).  
 1040 <https://doi.org/10.1016/j.jhydrol.2025.133160>
- 1041 Yang L., Smith J.A., Baeck M.L., Zhang Y. (2016). Flash flooding in small urban basins: storm event hydrologic response.  
 1042 *Water Resources Research*, 52 (6): 4571–4589. DOI: 10.1002/2015WR018326
- 1043 Yang, L., Smith, J., & Niyogi, D. (2019). Urban Impacts on Extreme Monsoon Rainfall and Flooding in Complex Terrain.  
 1044 *Geophysical Research Letters*, 46(11), 5918–5927. <https://doi.org/10.1029/2019GL083363>
- 1045 Zhou, Z., Smith, J. A., Baeck, M. L., Wright, D. B., Smith, B. K., & Liu, S. (2021). The impact of the spatiotemporal  
 1046 structure of rainfall on flood frequency over a small urban watershed: An approach coupling stochastic storm  
 1047 transposition and hydrologic modeling. *Hydrology and Earth System Sciences*, 25(9), 4701–4717.  
 1048 <https://doi.org/10.5194/hess-25-4701-2021>
- 1049 Zhu, Z., Wright, D. B., & Yu, G. (2018). The impact of rainfall space-time structure in flood frequency  
 1050 analysis. *Water Resources Research*, 54(11), 8983–8998. DOI: 10.1029/2018WR023550
- 1051 Ziaee, P., & Abedini, M. J. (2023). Investigating the Effect of Spatial and Temporal Variabilities of Rainfall on Catchment  
 1052 Response. *Water Resources Management*, 37(13), 5343–5366. <https://doi.org/10.1007/s11269-023-03610-0>
- 1053 Zoccatelli, D., Borga, M., Viglione, A., Chirico, G.B., Blöschl, G., (2011). Spatial moments of catchment rainfall: rainfall  
 1054 spatial organisation, basin morphology, and flood response. *Hydrol. Earth Syst. Sci.* 15 (12), 3767–3783.
- 1055 Zoccatelli, D., Borga, M., Zanon, F., Antonescu, B., & Stancalie, G. (2010). Which rainfall spatial information for flash  
 1056 flood response modelling? A numerical investigation based on data from the Carpathian range, Romania. *Journal*  
 1057 *of Hydrology*, 394(1–2), 148–161. <https://doi.org/10.1016/j.jhydrol.2010.07.019>

1058

1059

1060

1061

**Declaration of Generative AI and AI-assisted technologies in the  
writing process**

1062

1063

1064

1065

1066

1067

During the preparation of this work, the authors used AI-assisted technologies (Chat GPT, Claude) in order to improve readability and language. After using this tool/service, the authors reviewed and edited the content as needed and takes full responsibility for the content of the publication.

Journal Pre-proof

**Declaration of interests**

The authors declare that they have no known competing financial interests or personal relationships that could have appeared to influence the work reported in this paper.

The authors declare the following financial interests/personal relationships which may be considered as potential competing interests:

Journal Pre-proof